Tuning the properties of magnetic nanowires

L. Sun
Y. Hao
C.-L. Chien
P. C. Searson

Magnetic nanorods or nanowires exhibit degrees of freedom associated with their inherent shape anisotropy and the ability to incorporate different components along their length. The introduction of multiple segments along the length of a nanowire can lead to further degrees of freedom associated with the shape of each segment and the coupling between layers. In this paper, we present an overview of the magnetic properties of single-component and multiple-segment magnetic nanowires, and we provide examples of the influence of particle diameter, aspect ratio, and composition on many of their magnetic properties: the orientation of their magnetic easy axis, their Curie temperature, coercivity, saturation field, saturation magnetization, and remanent magnetization.

Introduction

Magnetic particles are being used—and being explored for use—in fields as diverse as biology and data storage. In these applications, the ability to control particle size, shape, composition, and surface chemistry is critical in obtaining the desired magnetic properties.

Suspensions of superparamagnetic particles are of interest in applications such as ferrofluidics [1, 2]. In biomagnetics, superparamagnetic particles are used commercially for cell sorting and are being explored for radiation treatment [3, 4]. Magnetic particles have been used in magnetic tweezers where the force required to displace magnetic particles bound to cells or proteins can be used to probe the micromechanics of cells [5] and the torsion of DNA molecules [6, 7]. Such particles are also being explored for use in drug delivery and gene therapy [8]. The use of magnetic field gradients to transport magnetic particles *in vivo* has been termed *magnetofection* [9, 10]. In magnetic data storage, the self-assembly of ferromagnetic particles is being explored for high-density magnetic media [11, 12].

In contrast to spherical particles, nanorods or nanowires exhibit degrees of freedom associated with their inherent shape anisotropy and their ability to incorporate different components along their length, as shown schemat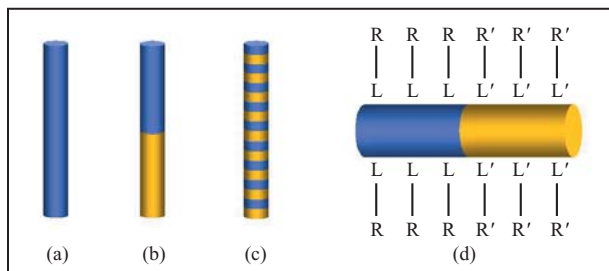ically in **Figure 1**. For example, ferromagnetic nanowires exhibit unique and tunable magnetic properties that are very different from those of bulk ferromagnetic materials, thin films, and spherical particles. The introduction of multiple segments along the length of a nanowire can lead to further degrees of freedom associated with the shape of each segment and the coupling between the layers.

The diverse range of applications has resulted in interest in nanoparticles with a wide range of magnetic properties. For example, the magnetic beads used in cell sorting are superparamagnetic in order to avoid aggregation; however, it is desirable that they have a relatively high magnetic moment so that they can be separated from the suspension at relatively low fields. In contrast, magnetic particles for magnetic recording should be ferromagnetic, with high saturation magnetization and high coercivity.

Both single-component and multiple-segment magnetic nanowires are of interest in these emerging fields, since magnetic properties such as the orientation of the magnetic easy axis, Curie temperature, coercivity, saturation field, saturation magnetization, and remanent magnetization can be tailored by modifying the diameter, composition, and layer thicknesses in multiple-segment FM/NM (FM = ferromagnetic, NM = nonmagnetic material) nanowires.

79

Schematic illustration of the inherent shape anisotropy associated with nanowires: (a) single-component nanowire; (b) two-component nanowire with segment aspect ratio >1; (c) two-component multilayer nanowire with segment aspect ratio <1; (d) functionalization of a two-component nanowire for which L and L′ represent ligands that bind selectively to the two components, and R and R′ represent spatially separated functional groups.

In response to the broad interest in the synthesis, manipulation, and magnetic properties of nanowires that now extends beyond physics to include chemistry and biology, in this paper we provide an overview describing how the magnetic properties of nanowires can be tuned by varying their size, shape, and composition.

Electrochemical template synthesis of nanowires

The deposition of structures, such as nanowires, with a high aspect ratio is difficult to achieve by vapor-phase techniques but is relatively straightforward using electrochemical template synthesis. Nanowires with diameters from 5 nm to more than 1 μm and with lengths up to 100 μm can be produced by electrochemical deposition into a nonconducting membrane having an array of parallel-sided pores. The electrochemical deposition of nanowire arrays was first reported [13, 14] in 1970 by Possin, who deposited tin nanowires in tracked mica films. Since then, this method has been used to fabricate nanowires of metals, alloys, semiconductors, and electronically conducting polymers [15–22]. The method involves the use of a metal film (sputtered onto one side of the membrane template) that serves as the working electrode (WE) in a conventional three-electrode electrodeposition cell, as shown in **Figure 2**. The nanowires form as the pores in the template are filled by the deposited material. This technique can also be used to synthesize multiple-segment nanowires, as illustrated in Figure 1. Another advantage of electrochemical template synthesis is that large quantities of monodisperse nanowires can readily be produced.

Templates for electrochemical deposition of nanowire arrays include porous anodized aluminum films [23–33], etched nuclear particle tracks in various materials [34–42],

and block copolymer films [43–45]. The properties of the nanoporous template, such as the relative pore orientations in the assembly, the pore size distribution, and the surface roughness of the pores, have significant influence on the intrinsic properties of the nanowires.

Nanoporous alumina templates are formed by anodic oxidation of aluminum [23–33]. Pore sizes typically range from 5 to 500 nm and up to about 200 μm in thickness, permitting the fabrication of nanowires with aspect ratios in excess of 1,000. Pore densities typically range from 10^8 to 10^{10} cm^{-2}. With careful preparation, relatively large domains of hexagonally ordered pores can be achieved. Longer-range ordering can be obtained by using stamping to seed pore locations [32, 33].

Nuclear track etching offers considerable flexibility in the choice of material, pore size, and template thickness [34–42]. Damage tracks are created in polymeric (e.g., polycarbonate) or inorganic (e.g., mica) insulating films by the passage of high-energy particles. With a suitable etchant, the etch rate of the damage tracks may be several orders of magnitude higher than that of the surrounding bulk material, so that uniform, parallel-sided pores can be created. Further etching results in enlargement of the pores at a rate determined by the bulk etch rate. Pore diameters are typically 10–1,000 nm, and pore densities of 1–10^9 cm^{-2} can easily be achieved. The disadvantage of this technique is that the pore distribution is inherently random. **Figure 3** shows a plan view scanning electron microscope (SEM) image of etched particle tracks in single-crystal mica.

Block copolymer templates have pore sizes ranging from 10 to 100 nm and pore densities ranging from 10^8 to 10^9 cm^{-2} [43–45]. The template thickness is limited but can be increased by annealing in the presence of an electric field, resulting in aspect ratios in excess of 100. Relatively large domains of close-packed nanopores can be obtained.

Ferromagnetic properties of nanowires

Magnetization hysteresis loops, which display the magnetic response of a magnetic sample to an external field, have been widely used to characterize the behavior of nanostructured magnetic materials. **Figure 4** shows typical magnetization hysteresis loops with the applied magnetic field parallel and perpendicular to the nanowire axis for an array of single-component ferromagnetic nanowires. The characteristic features of the hysteresis loop are dependent on the material, the size and shape of the entity, the microstructure, the orientation of the applied magnetic field with respect to the sample, and the magnetization history of the sample. For arrays of nanoparticles, the hysteresis loop may also depend on interactions between individual particles. The common parameters used to describe the magnetic properties
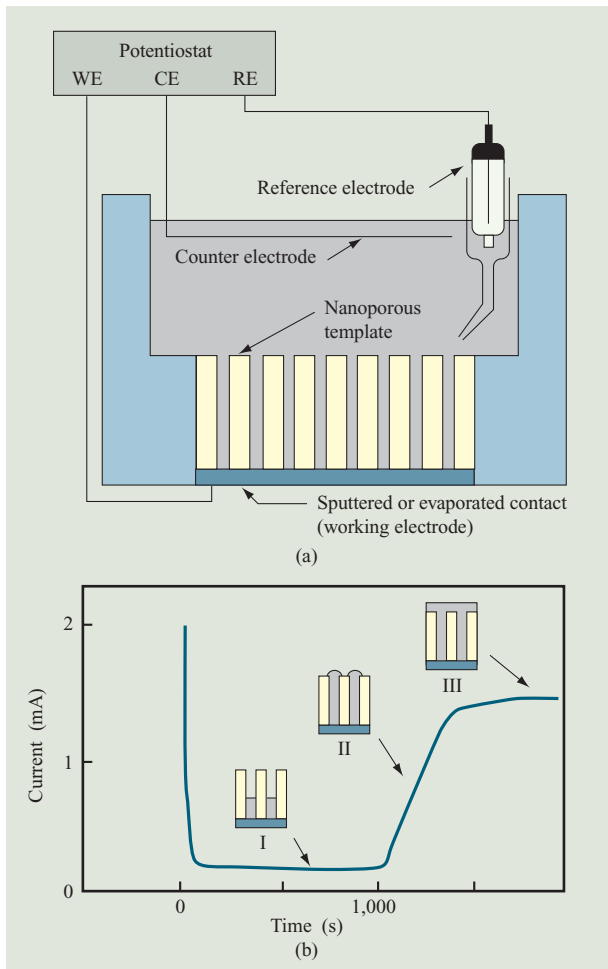
(a)

(b)

Figure 2

(a) Schematic illustration of cell for electrochemical deposition of nanowires. (b) Deposition current–time transient for deposition of 60-nm-diameter Ni nanowires in a 6-μm-thick polycarbonate template (pore density = 10^8/cm^2) from nickel sulfamate solution having a pH of 3.4. (WE: working electrode; CE: counter electrode; RE: reference electrode.) Adapted from [46], with permission.

Figure 3

Plan view SEM image of etched particle tracks formed in single-crystal mica. From [47], with permission.

(a)

(b)
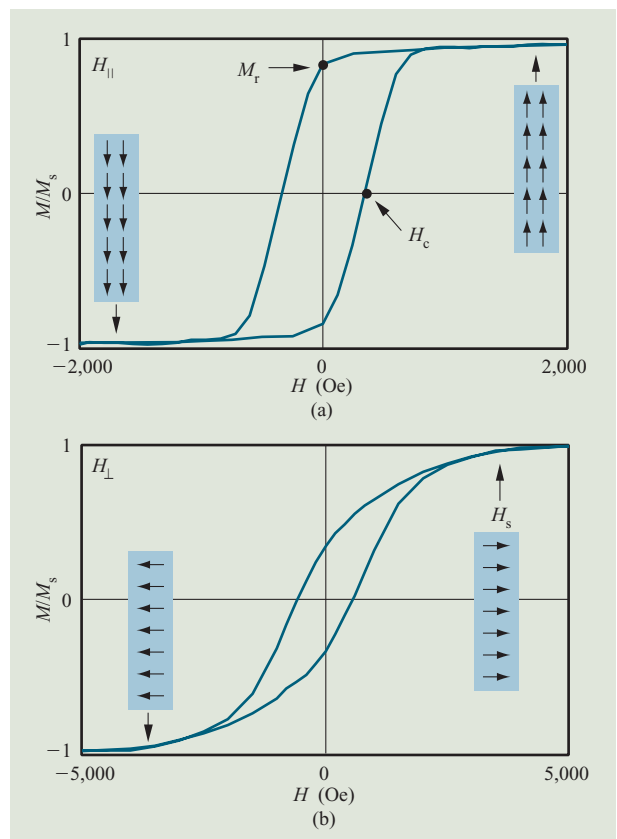
Figure 4

Typical hysteresis loops for an array of nickel nanowires 100 nm in diameter and 1 μm long with the applied field H parallel (a) and perpendicular (b) to the wire axis.

are the saturation magnetization M_s, the remanent magnetization M_r, the coercivity H_c, and the saturation field H_{sat}.

The coercivity H_c is the applied field at which the magnetization M becomes zero; the saturation field H_{sat} is the field needed to reach the saturation magnetization; and the remanent magnetization M_r is the magnetization at $H = 0$. For the case of magnetic nanowires, H_c, H_{sat}, and M_r are strongly dependent on the size and shape of the sample as well as the orientation of the applied magnetic field.

Another important parameter in describing the magnetic behavior of nanoparticles is the switching field H_s, which is the field needed to switch the magnetization
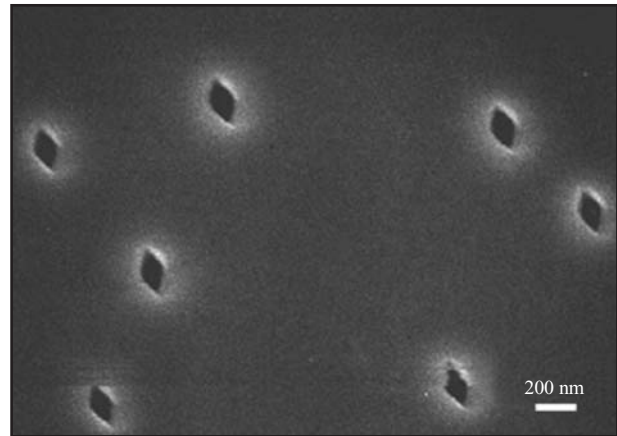
Table 1 Values of saturation magnetization for various materials.

Material	M_s (emu/cm^3) at 290 K
Fe	1,710
Ni	485
Co	1,440
bcc Fe$_{0.5}$Co$_{0.5}$ (permedur)	1,950
fcc Ni$_{0.78}$Fe$_{0.22}$	800

from one direction to the opposite direction. The switching field H_s can be defined as the field in which the slope of the M–H loop is maximum (i.e., $d^2M/dH^2 = 0$). As we describe in subsequent sections, in many cases of practical interest the switching field H_s is equal to the coercivity H_c. However, this is not always the case, as in the coherent rotation model when the applied field is oriented close to the magnetic hard axis. For an array of nanoparticles or nanowires, there is likely to be a distribution of switching fields due to small differences in size, shape, or microstructure. In this case, H_s characterizes nanowires with a switching field near the peak in the distribution. In many cases the switching field is symmetric (e.g., gaussian), and hence $H_s = H_c$.

The saturation magnetization M_s is obtained when all magnetic moments in the material are aligned in the same direction. M_s is a property of the ferromagnetic material and hence is independent of nanowire geometry. Values of the saturation magnetization in emu/cm^3 for different materials are given in **Table 1**.

As the temperature is increased, thermal fluctuations can overcome the ordering of the magnetic moments in a ferromagnetic material. The transition between ferromagnetic and paramagnetic behavior occurs at the Curie temperature T_c, which is a property of the material and is dependent on sample dimensions. For magnetic nanowires, all of these characteristic magnetic properties can be controlled by choice of material and dimensions.

In principle, magnetization hysteresis loops for an arbitrary entity can be calculated by minimizing the total free energy in the presence of an external field. The state of magnetization is determined from the eigenvalue of the magnetization vector configuration that minimizes the total system energy [48, 49]. The total energy E (erg/cm^3), can be expressed as

$$E = E_{ex} + E_H + E_{EA} + E_{ca} + E_D, \qquad (1)$$

where E_{ex} is the exchange energy, E_H is the Zeeman energy, E_{EA} is the magnetoelastic energy, E_{ca} is the crystalline anisotropy energy, and E_D is the magnetostatic energy (demagnetization energy).

The exchange energy E_{ex} is related to the interaction between spins that introduces magnetic ordering and can be written as

$$E_{ex} = -2 \sum_{i>j} J_{ij} S^2 \cos \theta_{ij}, \qquad (2)$$

where J_{ij} is the exchange integral, S is the spin associated with each atom, and θ_{ij} is the angle between adjacent spin orientations. For ferromagnetic materials, J is positive, and the minimum-energy state occurs when the spins are parallel to each other ($\theta_{ij} = 0$). Exchange interactions are inherently short-range and can be described in terms of the exchange stiffness constant A. The exchange stiffness is a measure of the force acting to keep the spins aligned and is given by $A = JS^2c/a$, where J is the exchange integral, S is the magnitude of the individual spins, c is a geometric factor associated with the crystal structure of the material ($c = 1$ for a simple cubic structure, $c = 2$ for a body-centered cubic structure, $c = 4$ for a face-centered cubic structure, and $c = 2\sqrt{2}$ for a hexagonal close-packed structure), and a is the lattice parameter. For most ferromagnetic materials, A is between 1×10^{-6} and 2×10^{-6} erg/cm (1×10^{-11} and 2×10^{-11} J/m).

The Zeeman energy E_H is often referred to as the magnetic potential energy, which is simply the energy of the magnetization in an externally applied magnetic field. The Zeeman energy is always minimized when the magnetization is aligned with the applied field; it can be expressed as

$$E_H = -\mathbf{M} \cdot \mathbf{H}, \qquad (3)$$

where $\mathbf{H}$ is the external field vector and $\mathbf{M}$ is the magnetization vector.

The magnetoelastic energy E_{EA} is used to describe the magnetostriction effect, which relates the influence of stress, or strain, on the magnetization of a material. For particles in suspension this effect can be neglected; however, in other cases it may be important.

The last two terms in Equation (1), the crystalline anisotropy energy E_{ca} and the magnetostatic energy (or demagnetization energy) E_D, describe the dependence of the total free energy on the direction of the magnetization with respect to lattice orientation and the shape of the sample, respectively. These two terms give rise to the size-dependent magnetic properties in nanostructures; they are discussed in more detail below.

Magnetocrystalline anisotropy

In a magnetic material, the electron spin is coupled to the electronic orbital (spin-orbital coupling) and influenced by the local environment (crystalline electric field). Because of the arrangement of atoms in crystalline materials, magnetization along certain orientations is energetically preferred. The magnetocrystalline

anisotropy is closely related to the structure and symmetry of the material.

For a cubic crystal, the anisotropy energy is often expressed [49] as

$$E_{ca} = K_0$$
$$+ K_1(\cos^2\theta_1\cos^2\theta_2 + \cos^2\theta_2\cos^2\theta_3 + \cos^2\theta_3\cos^2\theta_1)$$
$$+ K_2\cos^2\theta_1\cos^2\theta_2\cos^2\theta_3 + \cdots, \quad (4)$$

where K_0, K_1, K_2, $\cdots$ are constants (erg/cm^3) and θ_1, θ_2, and θ_3 are the angles between the magnetization direction and the three crystal axes, respectively. K_0 is independent of angle and can be ignored since it is the difference in energy between different crystal orientations that is of interest. In many cases, terms involving K_2 are small and can also be neglected. If $K_1 > 0$, E_{ca} is minimum in the $\langle 100 \rangle$ directions; hence, these directions are the easy axes. Conversely, if $K_1 < 0$, the easy axes correspond to the $\langle 111 \rangle$ directions. The difference in magnetocrystalline energy between the [111] direction and the [100] direction $\Delta K_{[111]-[100]}$ is equal to $K_1/3$. Similarly, the difference between the [110] direction and the [100] direction $\Delta K_{[110]-[100]}$ is equal to $K_1/4$.

The magnetocrystalline anisotropy energy associated with a hexagonal close-packed crystal is often expressed as

$$E_{ca} = K_0 + K_1\sin^2\theta + K_2\sin^4\theta, \quad (5)$$

where K_0, K_1, and K_2 are constants (erg/cm^3) and θ is the angle between the magnetization direction and the c-axis. As described above, K_0 is independent of angle. For most cases in which K_2 can be neglected, if $K_1 > 0$, the energy is smallest when $\theta = 0$, i.e., along the c-axis, so that this axis is the easy axis. If $K_1 < 0$, the basal plane is the easy axis. As a result of the symmetry of the hexagonal close-packed lattice, the magnetocrystalline anisotropy is a uniaxial anisotropy. Examples of K_1 for various materials are given in **Table 2**.

Shape anisotropy

The magnetization of a spherical object in an applied magnetic field is independent of the orientation of the applied field. However, it is easier to magnetize a nonspherical object along its long axis than along its short axis. If a rod-shaped object is magnetized with a north pole at one end and a south pole at the other, the field lines emanate from the north pole and end at the south pole. Inside the material the field lines are oriented from the north pole to the south pole and hence are opposed to the magnetization of the material, since the magnetic moment points from the south pole to the north pole. Thus, the magnetic field inside the material tends to demagnetize the material and is known as the demagnetizing field H_d. Stated formally,

Table 2 Values of the magnetocrystalline anisotropy energy constant K_1 for various materials.

Material	K_1 (erg/cm^3)
fct Co$_{0.5}$Pt$_{0.5}$	5×10^7
fcc Ni (easy axis [111])	-4.5×10^4
bcc Fe (easy axis [100])	4.8×10^5
fcc Ni$_{0.78}$Fe$_{0.22}$	0
hcp Co (easy axis [0001])	4.5×10^6

the demagnetizing field acts in the opposite direction from the magnetization **M** which creates it, and is proportional to it, namely

$$\mathbf{H}_d = -N_d\mathbf{M}, \quad (6)$$

where N_d is the demagnetizing factor. N_d is dependent on the shape of the body, but can only be calculated exactly for an ellipsoid where the magnetization is uniform throughout the sample. The magnetostatic energy E_D (erg/cm^3) associated with a particular magnetization direction can be expressed as

$$E_D = \frac{1}{2}N_d\mathbf{M}_s^2, \quad (7)$$

where M_s is the saturation magnetization of the material (emu/cm^3), and N_d is the demagnetization factor along the magnetization direction.

For a general ellipsoid with $c \geq b \geq a$, where a, b, and c are the ellipsoid semi-axes, the demagnetization factors along the semi-axes are N_a, N_b, and N_c, respectively. The demagnetization factors are related by the expression $N_a + N_b + N_c = 4\pi$.

Figure 5 shows three ellipsoids of particular interest in the study of nanowires: the prolate spheroid (or ellipsoid of revolution), slender ellipsoid, and oblate spheroid:

- *Prolate spheroid* (where $c > a = b$). This ellipsoid is of interest as an approximation for a single-component nanowire with circular cross section. When the aspect ratio is defined as $m = c/a$, its demagnetization factors are given by

$$N_a = N_b$$
$$= 4\pi\frac{m}{2(m^2-1)}$$
$$\times \left[m - \frac{1}{2(m^2-1)^{1/2}} \times \ln\left(\frac{m+(m^2-1)^{1/2}}{m-(m^2-1)^{1/2}} \right) \right]$$
$$\quad (8)$$

and
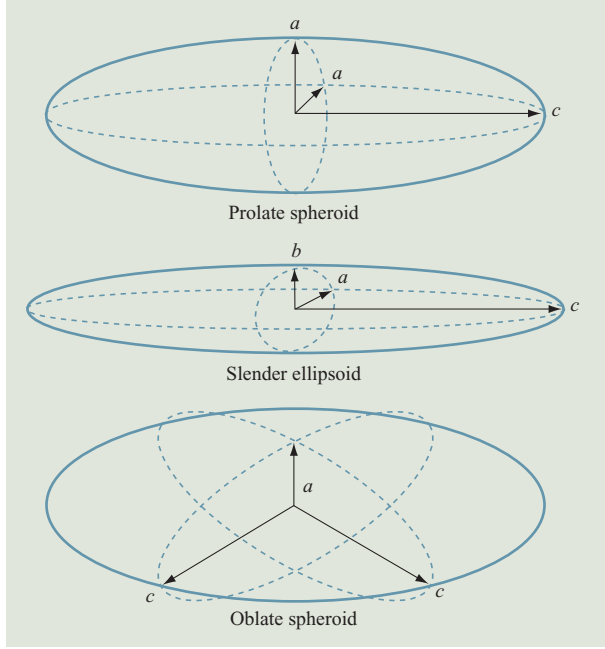
Figure 5

Schematic illustration of ellipsoids that are of particular interest in the study of nanowires.

Figure 6

Calculated dependence of the demagnetization factor ($N_d/4\pi$) of a prolate spheroid on its aspect ratio c/a. For $c/a > 10$, $N_a/4\pi \approx 0.5$ or $N_a \approx 2\pi$.

$$N_c = 4\pi \frac{1}{m^2 - 1}$$
$$\times \left[\frac{m}{2(m^2 - 1)^{1/2}} \times \ln\left(\frac{m + (m^2 - 1)^{1/2}}{m - (m^2 - 1)^{1/2}} \right) - 1 \right]. \quad (9)$$

- *Slender ellipsoid* (where $c \gg a > b$). This ellipsoid is of interest as an approximation for nanowires deposited into templates with noncircular cross sections, such as nanowires deposited in pores in single-crystal mica that have a diamond-shaped cross section. Its demagnetization factors are given by
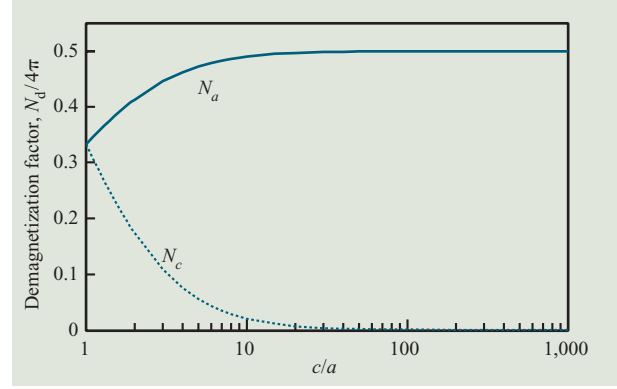
$$N_a = 4\pi \frac{b}{a+b} - \frac{1}{2}\frac{ab}{c^2} \ln\left(\frac{4c}{a+b} \right) + \frac{ab(3a+b)}{4c^2(a+b)}, \quad (10)$$

$$N_b = 4\pi \frac{a}{a+b} - \frac{1}{2}\frac{ab}{c^2} \ln\left(\frac{4c}{a+b} \right) + \frac{ab(a+3b)}{4c^2(a+b)}, \quad (11)$$

and

$$N_c = 4\pi \frac{ab}{c^2} \left[\ln\left(\frac{4c}{a+b} \right) - 1 \right]. \quad (12)$$

- *Oblate spheroid* (where $c = b > a$). This ellipsoid is of interest as an approximation for disk-shaped magnetic segments in multiple-segment nanowires. Defining the aspect ratio $m = c/a$, its demagnetization factors are given by

$$N_a = 4\pi \frac{m^2}{m^2 - 1} \left[1 - \frac{1}{(m^2 - 1)^{1/2}} \times \arcsin \frac{(m^2 - 1)^{1/2}}{m} \right] \quad (13)$$

and

$$N_b = N_c$$
$$= 4\pi \frac{1}{2(m^2 - 1)}$$
$$\times \left[\frac{m^2}{(m^2 - 1)^{1/2}} \times \arcsin \frac{(m^2 - 1)^{1/2}}{m} - 1 \right]. \quad (14)$$

Figure 6 shows the calculated dependence of the demagnetization factor ($N_d/4\pi$) of a prolate spheroid on its aspect ratio (c/a). A nanowire with a high aspect ratio (infinitely long cylinder) can be considered a prolate spheroid with a high aspect ratio (large c/a). In this case, the demagnetization factor along the hard axis, perpendicular to the wire axis, is equal to 2π, and the demagnetization factor along the easy axis, parallel to the wire axis, is 0. Thus, the shape anisotropy energy difference along the two axes obtained from Equation (7) is $K_u = \Delta E_D = E_{Da} - E_{Dc} = \pi M_s^2$. Note that the infinitely long cylinder approximation can be used for nanowires having an aspect ratio greater than about 10.

A disk-shaped ferromagnetic segment in a multiple-segment nanowire can be considered to be an oblate spheroid with a very low aspect ratio (small c/a). In this

case, the demagnetization factor N_a along the hard axis, parallel to the wire axis, is 4π, and the demagnetization factor N_c along the easy axis, perpendicular to the wire axis, is 0. Thus, the shape anisotropy energy difference along the two axes is $K_u = \Delta E_D = E_{Da} - E_{Dc} = -2\pi M_s^2$.

Saturation field

The saturation field H_{sat} is the external field needed to overcome the anisotropy energy and align the magnetic moments along the field direction. If we consider only shape anisotropy, from Equation (6) it can be seen that for a nanowire with a high aspect ratio ($N_a = 2\pi$ and $N_c = 0$), the saturation field parallel to the wire direction is 0, whereas the saturation field perpendicular to the wire axis is $2\pi M_s$. Referring to the M–H loops of Figure 4 (for 100-nm-diameter nickel nanowires with the applied field parallel and perpendicular to the wire axis), with the field parallel to the wire axis, the loop is relatively square, indicating that the magnetizations are easily aligned in this direction. The slight shearing of the curve is due to the fact that the pores in the polycarbonate templates are not all aligned perpendicular to the film plane. With the field perpendicular to the wire axis, the loop is sheared significantly. The field required to align the magnetizations perpendicular to the wire axis is about 3500 Oe, close to the value of $2\pi M_s = 3050$ Oe.

Switching in single-domain particles

In principle, the magnetization configuration in a magnetic nanowire can be determined from the Brown equation by minimizing the total free energy [50]. To simplify the problem, it is common to ignore the magnetoelastic energy (E_{EA}) and the crystalline anisotropy energy (E_{ca}). The magnetoelastic energy is usually very small for nanostructures. The crystalline anisotropy energy is important for single crystals or highly textured structures but is usually much smaller than the shape anisotropy. Other effects related to the microstructure and surface effects are also ignored. The remaining terms are analyzed by considering the collective spin motions. In bulk ferromagnetic materials, the energy of the system can be minimized by forming multiple magnetic domains in which the atomic magnetic moments are aligned. However, there is a critical size below which a particle remains in a single-domain state during switching.

For a prolate spheroid, the critical radius r_{sd} (in the short axis) for a single-domain particle can be expressed [50] as

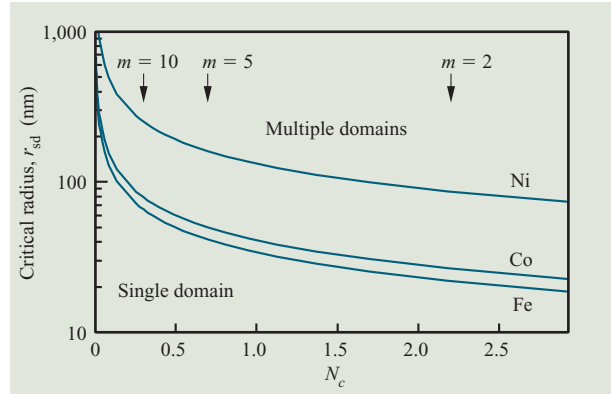$$r_{sd} = \sqrt{\frac{6A}{N_c M_s^2}\left[\ln\left(\frac{2r_{sd}}{a_1} - 1\right)\right]}, \qquad (15)$$

Figure 7

Critical radius for a single-domain prolate spheroid vs. demagnetization factor along the c-axis N_c from Equations (9) and (15). M_s(Ni) = 485, M_s(Co) = 1,440, M_s(Fe) = 1,710, a_1(Ni) = 0.2942 nm, a_1(Fe) = 0.2482 nm, and a_1(Co) = 0.2507 nm. In all cases $A = 1 \times 10^{-6}$ erg/cm.

where A is the stiffness constant (erg/cm), N_c is the demagnetization factor, M_s is the saturation magnetization (emu/cm^3), and a_1 is the near-neighbor spacing (cm). The critical radius for a single-domain particle is dependent on the materials parameters A, a_1, and M_s as well as the demagnetization factor N_c. Note that we use the near-neighbor spacing a_1 and that A contains the influence of the crystal structure. From **Figure 7** it can be seen that the critical radius should also increase with increasing aspect ratio ($m = c/a$) because of the decrease in the demagnetizing factor N_c. Thus, nickel nanowires with an aspect ratio of 10 ($N_c = 0.255$) would be expected to be single-domain nanowires for diameters less than about 600 nm ($r_{sd} \approx 300$ nm), whereas cobalt and iron nanowires with the same aspect ratio would be expected to be single-domain for diameters less than about 140 nm ($r_{sd} \approx 70$ nm).

For single-domain particles, the most common magnetization reversal modes can be modeled by *coherent rotation* or *curling*. In the absence of an applied field, the magnetic moments preferentially align along the easy axis, which is the longest major axis in an ellipsoid. In the coherent rotation model, all magnetic moments remain parallel to one another and rotate away from the easy axis during the reversal process, thus minimizing the exchange energy in the system. However, when there is a magnetization component along the hard axis, the demagnetization energy increases. In the curling model, neighboring magnetic moments are not constrained to be parallel, permitting the formation of configurations with no net magnetization along the hard axis and hence

85
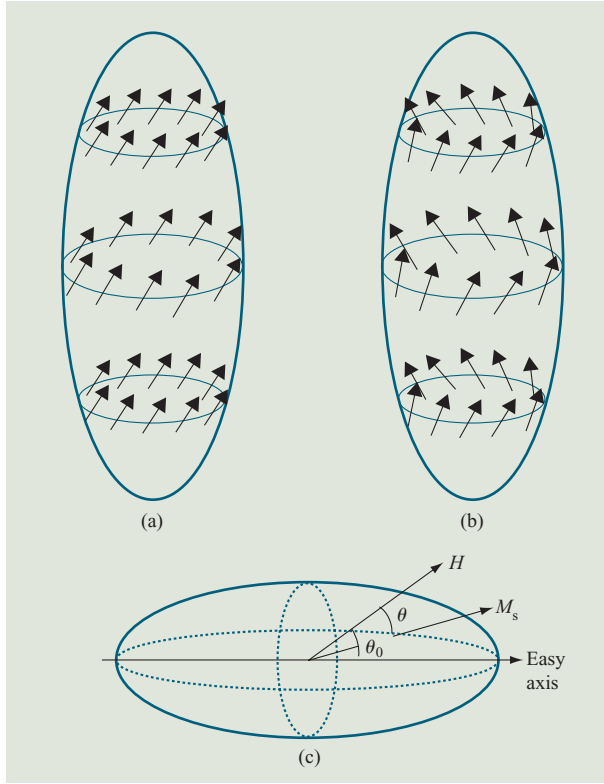
Figure 8

Illustrations of magnetization reversal in a single-domain prolate spheroid: (a) Coherent rotation; (b) curling; (c) coordinate system used for analysis of coherent rotation.

minimizing the demagnetization energy. However, if the magnetic moments are not parallel to one another, the exchange energy increases. Coherent rotation and curling are illustrated schematically in **Figure 8**.

The switching mode is determined by the competition between the exchange energy and the demagnetization energy. In the curling model, the exchange energy density increases with decreasing size because of the increase in relative angle between neighboring moments; hence, coherent rotation may become favorable. On the other hand, the demagnetization energy density increases with increasing aspect ratio, favoring curling. Thus, there is a critical size between the two magnetization reversal processes. When the magnetic easy axis is aligned with the applied field, the critical radius r_c (cm) for the transition is defined [51] by

$$r_c = q \left(\frac{2}{N_a} \right)^{1/2} \frac{A^{1/2}}{M_s},\tag{16}$$

where q is the smallest solution of the Bessel functions and is related to the aspect ratio of the prolate spheroid,

A is the exchange stiffness constant (erg/cm), M_s is the saturation magnetization (emu/cm^3), and N_a is the demagnetizing factor along the minor axis. The value of q varies between the limits of 1.8412 for a cylinder with an infinite aspect ratio and 2.0816 for a sphere with an aspect ratio of 1. For an infinitely long cylinder, $N_a = 2\pi$; hence, $r_c = (q/\sqrt{\pi})(A^{1/2}/M_s)$.

There are three terms, with different physical meanings, commonly used to describe the magnetization reversal process: the nucleation field H_n, which describes the field at which a change in magnetization just starts in a saturated single-domain state; the switching field H_s, which is the field at which an abrupt change in magnetization occurs; and the coercivity H_c, which is the field at which the magnetization changes sign. The nucleation field is a theoretical concept and is usually difficult to determine experimentally. Experimentally, the switching mechanism is usually determined from the angular dependence of the coercivity. Analytical solutions for the two reversal models with the external field applied at an angle θ_0 to the magnetic easy axis are summarized below.

Coherent rotation

In the classic *Stoner–Wohlfarth* (SW) coherent rotation model [52], the total free energy consists of the magnetostatic energy (or demagnetization energy) and the Zeeman energy due to the external magnetic field, viz.,

$$E = E_D + E_H.\tag{17}$$

The coordinate system used for the analysis of coherent rotation is shown in Figure 8. The magnetostatic energy for a prolate spheroid is given by the expression

$$E_D = K_u \sin^2(\theta - \theta_0),\tag{18}$$

where θ_0 is the angle between the external field and the magnetization easy axis, θ is the angle between the magnetization and the external field, and K_u is the uniaxial shape anisotropy constant. [Note that for a prolate spheroid with high aspect ratio ($N_a \approx 2\pi$ and $N_c \approx 0$), $K_u = \pi M_s^2$.] Recall from Equation (3) that $E_H = -\mathbf{H} \cdot \mathbf{M}$. The total magnetic energy can be written as

$$E = K_u \sin^2(\theta - \theta_0) - \mathbf{H} \cdot \mathbf{M}_s.\tag{19}$$

The component of the magnetization along the field axis is $M = M_s \cos\theta$; hence, Equation (19) can be written as

$$E = K_u \sin^2(\theta - \theta_0) - HM_s \cos\theta.\tag{20}$$

The total energy is minimized when $dE/d\theta = 0$; hence,

$$2K_u \sin(\theta - \theta_0)\cos(\theta - \theta_0) + HM_s \sin\theta = 0.\tag{21}$$

Using the reduced field $h = H/(2K_u/M_s)$, Equation (21) can be written as

$$\sin(\theta - \theta_0)\cos(\theta - \theta_0) = -h\sin\theta. \tag{22}$$

Recalling that $2\sin\alpha\cos\alpha = \sin 2\alpha$, we obtain

$$\sin[2(\theta - \theta_0)] = -2h\sin\theta. \tag{23}$$

For a given orientation of the external field θ_0, this equation defines the angle θ between the magnetization and the applied field for each value of h. Since $\sin(\alpha - \beta) = \sin\alpha\cos\beta - \cos\alpha\sin\beta$,

$$\sin 2\theta\cos 2\theta_0 - \cos 2\theta\sin 2\theta_0 = -2h\sin\theta. \tag{24}$$

Using the trigonometric relations $\sin 2\alpha = 2\sin\alpha\cos\alpha$, $\cos 2\alpha = 1 - 2\sin^2\alpha$, and $\sin\alpha = (1 - \cos^2\alpha)^{1/2}$, we obtain

$$2\cos\theta(1 - \cos^2\theta)^{1/2}\cos 2\theta_0 + (1 - 2\cos^2\theta)\sin 2\theta_0$$
$$= -2h\sin\theta. \tag{25}$$

The reduced magnetization $m = M/M_s$, and since $M = M_s\cos\theta$, we can see that $m = \cos\theta$. Thus, the general solution relating the magnetization m to the applied field h at a specific angle θ_0 to the easy axis is

$$2m(1 - m^2)^{1/2}\cos 2\theta_0 + (1 - 2m^2)\sin 2\theta_0$$
$$= \pm 2h(1 - m^2)^{1/2}. \tag{26}$$

The magnetization hysteresis loop can be calculated from this equation by solving for m as a function of h. The switching field can be obtained when

$$\frac{\partial h}{\partial m} = 0 \text{ and } \frac{\partial^2 E}{\partial \theta^2} > 0 \tag{27}$$

and can be written as

$$h_s = (\cos^{2/3}\theta_0 + \sin^{2/3}\theta_0)^{-3/2}, \tag{28}$$

where $h_s = H_s/(2K_u/M_s)$.

The switching angle, i.e., the angle at which the magnetization flips, can be obtained from

$$\tan^3(\theta_0 - \theta_s) = -\tan\theta_0. \tag{29}$$

Figure 9 shows m vs. h curves for the coherent rotation model. For a given value of θ_0, the m–h loop is calculated in the following way. First h_s and θ_s are determined from Equations (28) and (29). Equation (23) is then used to calculate θ at each value of h. Finally, the relation $m = \cos\theta$ is used to calculate the m vs. h curve. The calculation is divided into two regions corresponding to the positive-going branch and the negative-going branch of the m–h loop, starting from $h = 1.5$ to $h = -1.5$: 1) $1.5 > h > -h_s$, with θ restricted to values between $0°$ and θ_s, and 2) $-h_s > h > 1.5$, with θ restricted to values between $180°$ and $180° + \theta_0$.

In this model, two regimes can be identified on the basis of the dependence of the switching field (h_s) and coercive field (h_c) on the angle (θ_0) between the external
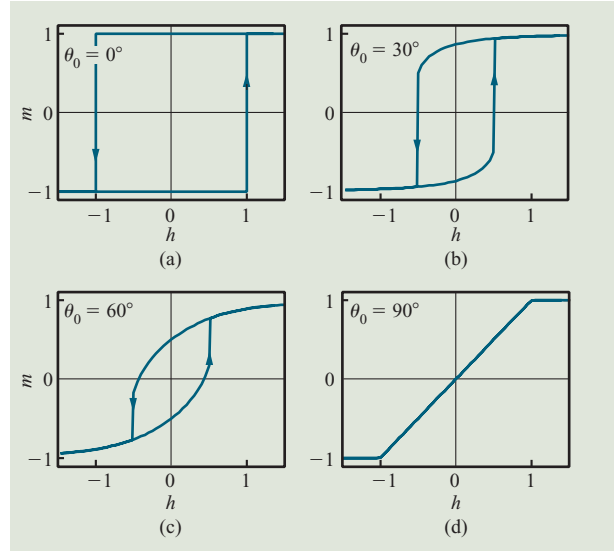
Calculated m–h curves for the coherent rotation model assuming an applied field at an angle θ_0 with respect to the magnetization easy axis (nanowire axis). The predicted behavior is shown for $\theta_0 = 0°$, $30°$, $60°$, and $90°$.

field and the magnetization easy axis (nanowire axis). When the applied field is close to the magnetic easy axis, $0° < \theta_0 < 45°$, the hysteresis loop is relatively square; hence, the change in sign of the magnetization, corresponding to the coercivity, occurs at the switching field. In this regime the coercivity H_c is equal to H_s and is determined from Equation (28).

For $45° < \theta_0 < 90°$, the applied field is oriented closer to the magnetic hard axis, and the hysteresis loop is sheared such that switching occurs after the magnetization changes sign. In this case, $H_c \neq H_s$, and the coercive field is determined from Equation (26) by setting $m = 0$, leading to the expression

$$h_c = \sin\theta_0\cos\theta_0, \tag{30}$$

where $h_c = H_c/2(K_u/M_s)$.

Figure 10 shows the angular dependence of the reduced switching field h_s and reduced coercivity h_c, according to Equations (28) and (30), respectively. Comparison of the two figures shows that $h_s = h_c$ when $0 < \theta_0 < 45°$, whereas for $45° < \theta_0 < 90°$, $h_s \neq h_c$.

A key feature of the coherent rotation model, as seen from Equations (28) and (30), is that the switching field and coercivity are independent of particle size.

Curling

For particle sizes larger than the critical size but still in the single-domain regime, magnetization reversal

87

L. SUN ET AL.
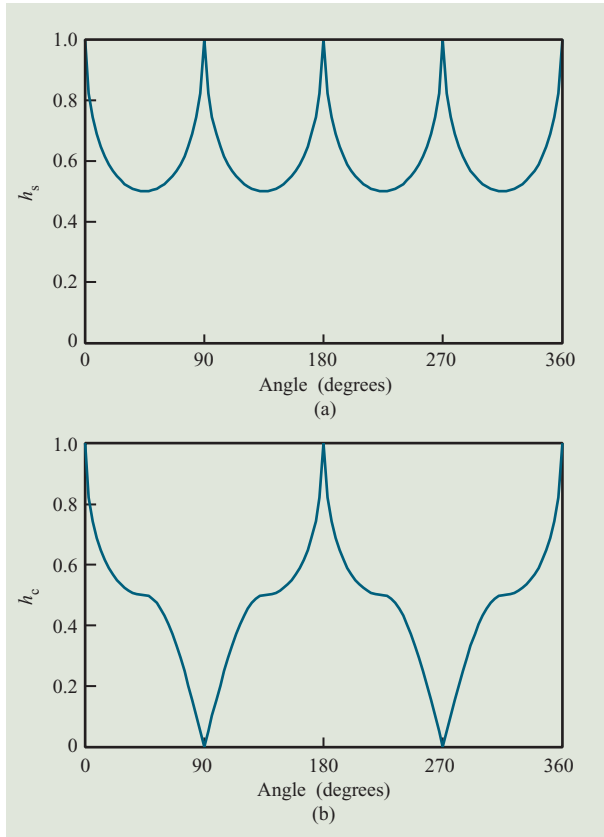
Figure 10

Calculated angular dependence of (a) the reduced switching field h_s and (b) the reduced coercivity h_c for the coherent rotation model, from Equations (28) and (30). In both cases the fields are normalized by the factor $2K_u/M_s$.

occurs by curling [50, 53–55]. In the curling model, magnetization switching is an abrupt process, and the switching field is very close to the nucleation field; hence, $H_c = H_s$ for all angles. Furthermore, H_c and H_s are dependent on both the aspect ratio and the size of the ellipsoid [55].

Analytical solutions for m vs. h curves in the curling model are not available. The angular dependence of the normalized nucleation field for a prolate spheroid based on the curling model is given [53] by

$$h_c(\theta) = \frac{\left(2N_c - \dfrac{k}{S^2}\right)\left(2N_a - \dfrac{k}{S^2}\right)}{\sqrt{\left(2N_c - \dfrac{k}{S^2}\right)^2 \sin^2\theta + \left(2N_a - \dfrac{k}{S^2}\right)^2 \cos^2\theta}}, \quad (31)$$

where $h_c = H_c/2\pi M_s$, N_c and N_a are the demagnetizing factors of the spheroid along the major and minor axes; S is the reduced radius r/r_0, where $r_0 = A^{1/2}/M_s$; $k = q^2/\pi$, where q is the same geometrical factor used in Equation

(16) ($q = 1.8412$ for a cylinder and 2.0816 for a sphere); and θ is the angle between the external magnetic field and the magnetic easy axis (c-axis). Note that r_0 is independent of the size and shape of the spheroid and is related to the critical size for the transition between curling and coherent rotation via $r_c/r_0 = q/\sqrt{\pi}$.

Figure 11 shows the angular dependence of the coercivity of a slender spheroid with high aspect ratio ($q = 1.8412$, $N_c = 0$, and $N_a = 2\pi$) predicted by the curling model [calculated using Equation (31)] as a function of diameter and aspect ratio. The corresponding angular dependence of the coercivity from the coherent rotation model is shown for comparison. The figure illustrates that the angular dependence of the normalized coercivity predicted by the curling model is opposite to that predicted by the coherent rotation model. Just as the magnetization configuration adopts the lowest-energy
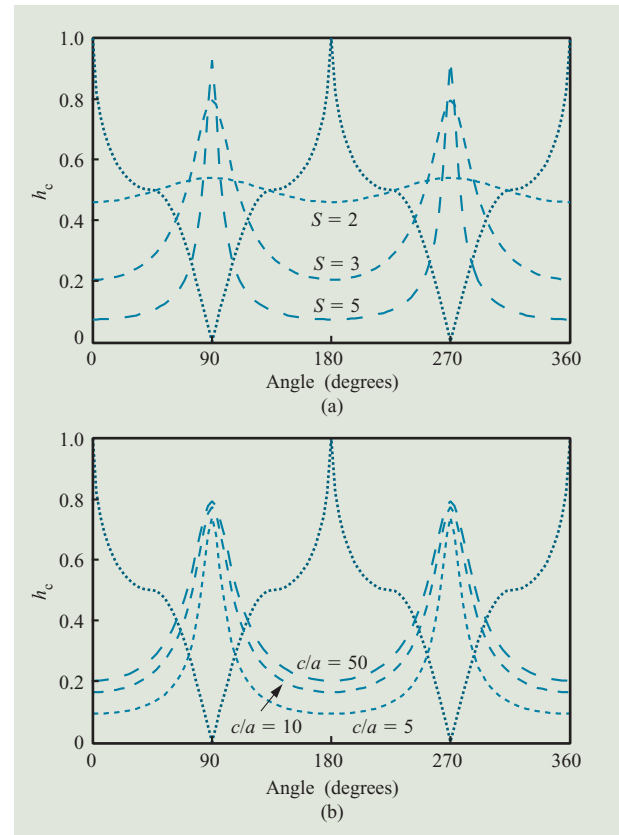
Figure 11

Calculated angular dependence of the reduced coercivity $h_c = H_c/2\pi M_s$ based on the curling model, from Equation (31): (a) Dependence on nanowire diameter $S = r/r_c$, assuming $c/a = 10$; (b) dependence on aspect ratio c/a assuming $S = 3$. The angular dependence of the coercive field calculated via the coherent rotation model for an infinitely long cylinder is also shown (dotted curves).

state, switching occurs by the process that gives the lowest coercivity. At lower angles, for which the applied field is aligned closely with the easy axis (along the wire axis), switching will occur by curling if the nanowire diameter is larger than the critical size $[r > r_c(\theta)]$. Note that Equation (16) describes the critical radius only when the applied field is aligned along the wire axis ($\theta = 0$). However, at higher angles, switching is predicted to occur by coherent rotation. The calculated angle at which the switching mode changes from curling to coherent rotation increases for larger wire diameter and lower aspect ratio.

For an applied field oriented along the magnetic easy axis (c-axis), for which $\theta = 0$, Equation (31) can be expressed as

$$h_c = \frac{\left(2N_c - \dfrac{k}{S^2}\right)\left(2N_a - \dfrac{k}{S^2}\right)}{\left|2N_a - \dfrac{k}{S^2}\right|}. \tag{32}$$

For a prolate spheroid with a high aspect ratio, $N_c = 0$ and $N_a = 2\pi$; hence, Equation (32) reduces to

$$h_c = \frac{k}{S^2}. \tag{33}$$

For an infinitely long cylinder, $q = 1.8412$; and recalling that $k = q^2/\pi$ and $S = r/r_0$,
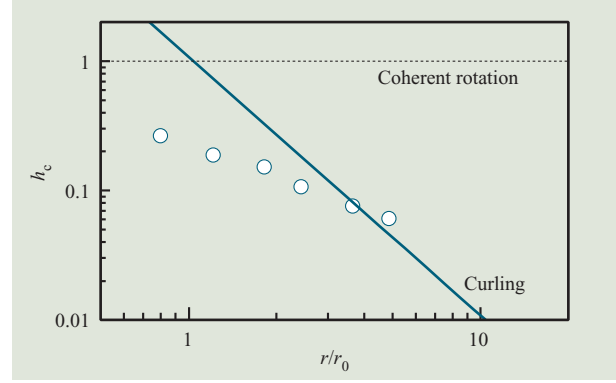
$$h_c = 1.08\frac{1}{(r/r_0)^2}. \tag{34}$$

Thus, according to the curling model, the coercivity of a nanowire is expected to increase with $1/r^2$. **Figure 12** shows the reduced nucleation field (or coercivity) vs. reduced radius, as predicted by Equation (34). This figure suggests that in the curling regime the coercivity of nanowires can be significantly increased by decreasing the wire diameter. The figure also includes measurements that are discussed later (in the section on experimental results).

Superparamagnetism

At finite temperatures, the process of magnetization reversal can be viewed as overcoming a single energy barrier. Thermal fluctuations can allow the magnetization of a sample to surmount the energy barrier and switch from one stable direction to the other. The switching probability per unit time P (s^{-1}) can be obtained from the Arrhenius relation,

$$P = v_0\exp\left(-\frac{\Delta E}{kT}\right), \tag{35}$$

where v_0 is the thermal attempt frequency, which is usually assumed to be 10^9 s^{-1} [56]; ΔE is the energy barrier; k is the Boltzmann constant; and T is the temperature. A reversing field aligned in the opposite direction from the magnetization direction acts to lower

the energy barrier, thereby increasing the probability of switching. The dependence of the applied field on the energy barrier is often described [57] by the expression

$$\Delta E = U\left(1 - \frac{H}{H_0}\right)^{1/n}, \tag{36}$$

where U is the energy barrier at zero applied field, H is the applied field, and H_0 is the field needed to overcome the barrier at zero temperature. The parameter n reflects different switching mechanisms.

If we assume that the switching field H_s is equal to H_c and take the coercivity as the applied field at which the probability of switching in a time t is 0.5, by combining Equations (35) and (36) we obtain

$$H_c(t, T) = H_0\left[1 - \left(\frac{kT}{U}\ln(2f_0 t)\right)^n\right]. \tag{37}$$

This equation indicates that the parameter n and energy barrier U can be obtained by measuring the time dependence and temperature dependence of the coercivity. This has become the standard method for measuring the thermal stability of an assembly of magnetic particles.

For single-domain particles having a uniaxial shape anisotropy, the energy barrier is just the energy required to switch by coherent rotation. Thus, the barrier is equal to $K_u V$, where K_u is the uniaxial shape anisotropy constant and is equal to $M_s(N_a - N_b)$, and V is the

89
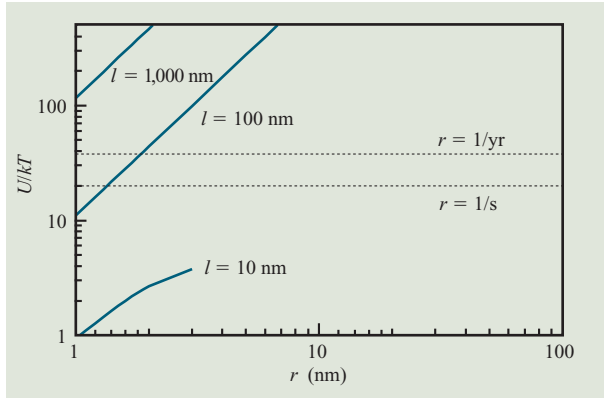
Figure 13

Calculated dependence of the energy barrier for spontaneous switching on nanowire radius calculated from $U = K_u V$, assuming that $K_u = (N_a - N_c)M_s^2$ and $M_s = 485$ emu/cm³. The dotted lines correspond to switching probabilities of one per second and one per year, respectively.

particle volume. H_0 and ΔE can be rigorously derived as follows:

$$H_0 = \frac{2K_u}{M_s}; \tag{38}$$

$$\Delta E = K_u V \left(1 - \frac{H}{H_0}\right)^2. \tag{39}$$

For more complex switching mechanisms, such as curling, the following equations have been adopted for characterizing an assembly of randomly oriented single-domain magnetic particles [58]:

$$H_0 = \frac{2K_{\text{eff}}}{M_s}; \tag{40}$$

$$\Delta E = K_{\text{eff}} V \left(1 - \frac{H}{H_0}\right)^{3/2}, \tag{41}$$

where the switching volume V might be a fraction of the particle volume, the portion that must rotate in order to initiate the reversal process of the entire particle. K_{eff} is called the effective anisotropy constant; it reflects the combined effect of all of the applicable energy terms on the magnetization rotation process.

Since in general the energy barrier for magnetization switching in a particle is proportional to the particle volume, a particle with volume below a critical value would not have an energy barrier high enough to prevent spontaneous switching at room temperature resulting from thermal fluctuations (characterized by an energy

equal to kT). The particle behaves like a paramagnetic material, but with a much higher susceptibility. This phenomenon, called *superparamagnetism*, has become of considerable interest in high-density magnetic recording media. For a particle to retain its magnetization at room temperature (298 K) on average, for $t = 1$ s, $U \approx 21kT$; hence, if $U < 21kT$, we regard the particle as being superparamagnetic at room temperature.

For magnetic nanowires, an estimate for the energy barrier in the remanent state ($H = 0$) can be determined by assuming $K_{\text{eff}} = K_u$ (shape anisotropy). For a prolate spheroid, $K_u = (N_a - N_c)M_s^2$, provided the aspect ratio $c/a > 10$. In that case $N_a = 2\pi$ and $N_c = 0$, so that $K_u = 2\pi M_s^2$ (see Figure 6). On the basis of this assumption, **Figure 13** shows the dependence of the energy barrier on radius for nickel nanowires as a function of their length. For magnetic recording media, stability over a time scale of ten years is usually required, giving a criterion of $U/kT > 40$. The energy barrier for nickel nanowires with radii larger than about 2 nm and more than 100 nm in length is sufficiently large to satisfy this criterion. For particles in suspension that have been magnetized, magnetostatic interactions may lead to aggregation. The figure shows that short nickel nanorods 10 nm in length would be expected to be superparamagnetic for radii less than about 10 nm, since the switching probability is close to 1 for a time period of one second. Consequently, aggregation induced by magnetic interactions should not be significant, resulting in a stable suspension.

Magnetostatic interactions between nanowires

In the discussions above, we have assumed that the magnetostatic interaction between nanowires is negligible. The magnetic field H_x created by a dipole with moment m and length l, at distance x in the direction perpendicular to the dipole, is given [59] by

$$H_x = \frac{m}{\left(x^2 + \frac{l^2}{4}\right)^{3/2}}, \tag{42}$$

where the magnetic moment $m = M_s V$, and l and r are respectively the length and radius of the dipole. This dipole approximation gives a valuable estimation of the magnitude of the magnetostatic interaction between nanowires. **Figure 14** shows a plot of the field H_x at a distance x from a cylindrical nickel nanowire ($M_s = 485$ emu/cm³). For a nanowire having a radius of 100 nm, the field is calculated to be about 110 Oe within 100 nm but to decrease to small values at about 1 μm. For longer nanowires, the maximum field is calculated to decrease significantly. The field for smaller-

diameter nanowires is calculated to be significantly smaller and to drop off at shorter distances. Since the coercivity of nickel nanowires is typically 100–1000 Oe, magnetostatic interactions are expected to be important only for larger-diameter nanowires that are closely spaced, as would be typical in alumina templates [59, 60].

Experimental results

The magnetic properties of a wide range of single-component [46, 47, 61–75] ferromagnetic nanowires have been studied. **Figure 15** shows M–H loops for 120-nm-diameter nickel nanowires in a single-crystal mica template [47]. A plan view image of a single-crystal mica template formed by nuclear track etching was shown in Figure 3 [42]. The pores have a diamond-shaped cross section with angles of 60° and 120°. The pore density is controlled by the flux of high-energy particles passing through the membrane, and the pore size is controlled by the etching time. The etching rate along the particle track is more than three orders faster than the lateral etching rate, resulting in uniform, parallel-sided nanopores perpendicular to the film plane. The axes of the pores are aligned by collimation of the irradiation source. The crystal structure of mica determines the etching anisotropy. For convenience, we define an effective diameter of a pore as the diameter of a circle with same area.

The magnetization hysteresis loop obtained with the applied field parallel to the wire axis is relatively square, characteristic of the easy axis, with a remanence M_r/M_s of 0.89. Since the pores have a diamond-shaped cross section, the nanowires exhibit magnetic anisotropy in the plane perpendicular to the wire axis, as shown in Figure 15. Rotating the field from along the short diagonal a to along the long diagonal b results in a decrease in the saturation field from 4650 Oe to 3380 Oe, as shown in the figure. Concurrently, the coercivity decreases from 220 Oe to 80 Oe, and the squareness of the loop decreases from 0.066 to 0.056.

Figure 16 shows the dependence of the coercivity (H_c) and loop squareness on the effective nanowire diameter with the applied field parallel to the wire axis. In order to maintain approximately the same volume fraction of nickel ($\approx 2\%$) in all samples, the nanowire density was increased from 5×10^7 cm^{-2} for the 200-nm pores to 2×10^9 cm^{-2} for the 30-nm pores. The average wire spacing decreased from 1.4 μm for the 200-nm-diameter nanowires to 220 nm for the 30-nm-diameter nanowires. The measured coercivity [Figure 16(a)] increases with decreasing diameter, reaching a value of 800 Oe at an effective wire diameter of 30 nm. Figure 16(b) shows the magnitude of the remanent magnetization obtained from the hysteresis loops and plotted as the squareness (SQ), defined as the ratio of remanence to saturation
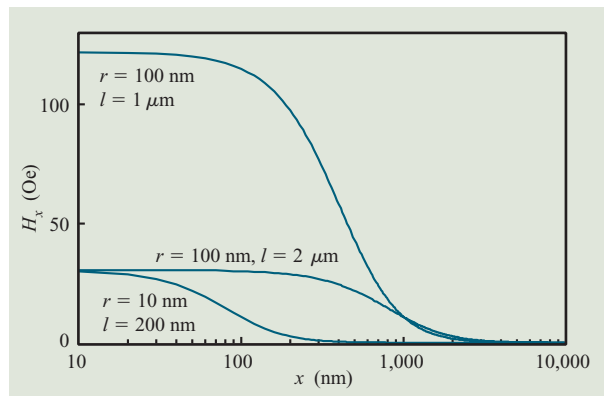
Magnetic field at a distance x from a nickel nanowire ($M_s = 485$ emu/cm³) of radius r and length l, calculated from Equation (42).
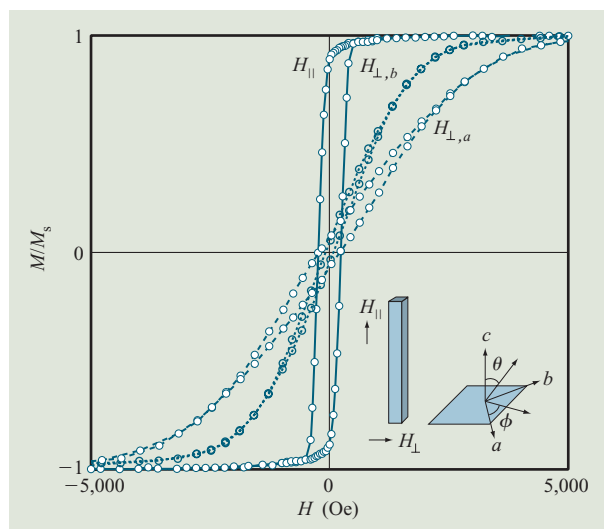
Typical M–H loops for nickel nanowires with an effective pore diameter of 120 nm; magnetic field applied parallel ($H_{||}$) and perpendicular ($H_\perp$) to the wire axes. Adapted from [46], with permission.

magnetization ($SQ = M_r/M_s$). The value of SQ is as high as 0.96 for the 30-nm-diameter wires, decreasing gradually to 0.83 for the 200-nm-diameter wires. Both the coercivity and the squareness of nanowires grown in a mica membrane are larger compared with those grown in a polymer membrane having the same diameter [46, 68, 69]. These enhancements can be attributed directly to the improved collimation of the pores, the uniform pore cross section, and the low density of overlapping pores.

91
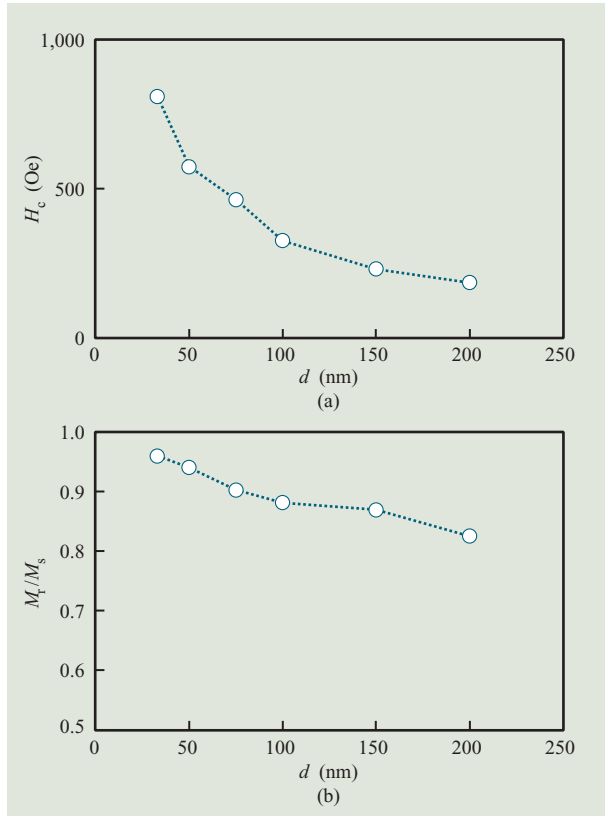
Figure 16

(a) Coercivity and (b) squareness of hysteresis loop for nickel nanowire arrays in single-crystal mica films as a function of the effective wire diameter measured along the wire axis. Adapted from [70], with permission.
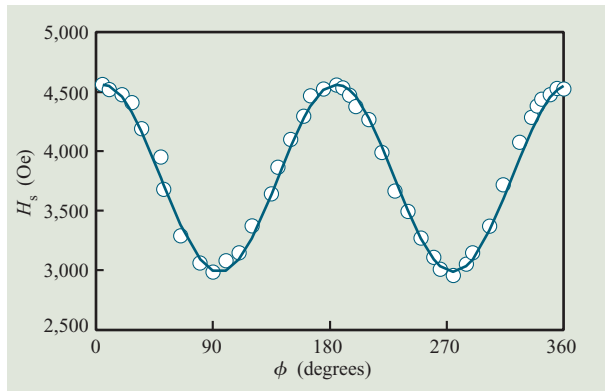
Figure 17

Angular dependence of the saturation field for 120-nm-diameter nickel nanowires with the external field perpendicular to the wire axis. $\phi = 0°$ corresponds to the short diagonal. The solid curve depicts Equation (45), assuming appropriate values of parameters. Adapted from [47], with permission.

The in-plane magnetization anisotropy can be discussed qualitatively on the basis of the slender ellipsoid approximation with demagnetization factors along three axes defined as N_a, N_b, and N_c. From Equations (6) and (7), the magnetic shape anisotropy energy is the total demagnetization energy if no other anisotropy is considered. The magnetization energy can be written as the sum of the demagnetization energy along the three axes, viz.,

$$E = \frac{1}{2}(N_a M_a^2 + N_b M_b^2 + N_c M_c^2)$$
$$= \frac{1}{2}M_s^2(N_c \cos^2\theta + N_a \sin^2\theta\cos^2\phi + N_b \sin^2\theta\sin^2\phi),$$
(43)

where θ is the angle between the magnetization and the wire axis (c-axis), and ϕ is the angle between the in-plane projection of the magnetization and the short diagonal of the cross section (a-axis).

When the magnetization is aligned in the *ab* plane ($\theta = 90°$), Equation (43) reduces to

$$E = \frac{1}{2}M_s^2(N_a \cos^2\phi + N_b \sin^2\phi)$$
$$= K_a \cos^2\phi + K_b \sin^2\phi,$$
(44)

where K_a and K_b are the uniaxial anisotropy constants along the *a* and *b* directions. From this expression, we can write the saturation field as

$$H_{\text{sat}} = M_s(N_a \cos^2\phi + N_b \sin^2\phi)$$
$$= \frac{2K_a}{M_s}\cos^2\phi + \frac{2K_b}{M_s}\sin^2\phi.$$
(45)

Figure 17 shows the agreement obtained between the measured angular dependence of the saturation field and Equation (45). From the fit, we obtain $K_a = 1.13 \times 10^6$ erg/cm^3 and $K_b = 8.2 \times 10^5$ erg/cm^3. The corresponding demagnetizing factors are $N_a = 0.764$ and $N_b = 0.556$. These values can be compared to the calculated demagnetizing factors for a slender ellipsoid with $c/a = 43.8$ and $c/b = 25.3$ [Equations (10) and (11)], of $N_a = 0.633$ and $N_b = 0.365$ [47]. These values are in reasonable agreement given the difference in cross section between a diamond and an ellipse. Thus, the in-plane shape anisotropy caused by the diamond-shaped cross section can be described by a simple model based on two mutually perpendicular anisotropic axes.

We now discuss the magnetization when the external field is rotated from the direction parallel to the wire axis ($\theta = 0°$) to being perpendicular to the wire axis ($\theta = 90°$) in the *ac* or *bc* plane. When $H = 0$, the magnetizations in the nanowires are aligned along the c-axis (the magnetic easy axis). However, the magnetization is measured at an angle θ with respect to the c-axis. Thus, the component of the remanent magnetization $M_r(\theta)$ at an angle θ

to the c-axis is cos θ. Therefore,

$$M_r(\theta) = M_r(\theta = 0)|\cos\theta|, \qquad (46)$$

where $M_r(\theta = 0)$ is the remanent magnetization when the applied field is along the wire axis ($\theta = 0°$). **Figure 18** shows that the remanent magnetization of the hysteresis loops decreases with increasing θ according to Equation (46).

The critical radius r_c between coherent rotation and curling for an infinitely long nickel cylinder obtained from Equation (16) is 20 nm. Thus, switching in nickel nanowires is expected to occur by curling. As was shown in Figure 16, the easy-axis coercivity increases with decreasing diameter, as is consistent with the curling model. Measured values for the normalized coercivity vs. the normalized nanowire radius using $A = 1 \times 10^6$ erg/cm^3 and $M_s = 485$ erg/cm^3 were shown in Figure 12. For larger-diameter nanowires, the coercivity shows good agreement with the curling model; however, at smaller diameters the coercivity does not increase as rapidly as predicted by the model. Similar results have been reported for cylindrical Ni nanowires in porous alumina templates [67]. As described above, the earlier magnetization reversal models take into account only shape anisotropy. For smaller-diameter wires, magnetization nonuniformity can cause noncoherent switching and result in a smaller coercivity than predicted by the model.

Figure 19 shows the angular dependence of the coercivity measured in the ac and bc planes for 120-nm-diameter Ni nanowires. The coercivity initially increases with increasing angle, in good agreement with the curling model; however, there is a critical angle above which H_c decreases abruptly. For nanowires having a size larger than the critical size, the coercivity due to curling is lower than for coherent rotation when the applied field is along the wire axis. However, since the angular dependences of the two reversal modes have opposite trends, at higher angles, reversal by coherent rotation may occur via a lower coercivity. Thus, for a given particle diameter and aspect ratio, there exists a critical angle at which the magnetization reversal modes change from curling to coherent rotation. For a constant diameter, the critical angle increases with increasing aspect ratio. For a constant aspect ratio, the critical angle decreases with decreasing particle diameter. As our measurements on the prismatic Ni nanowires indicate, the transition from curling to coherent rotation occurs at about 78° when the field is aligned in the ac plane but increases to about 85° when the field is aligned in the bc plane.
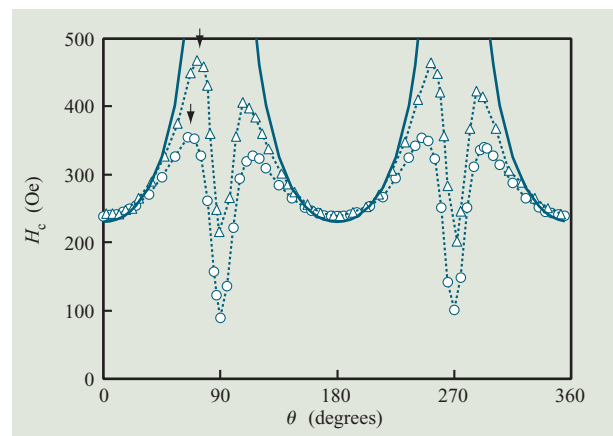
Curie temperature

Superparamagnetic behavior describes the influence of thermal fluctuation on small magnetic particles that
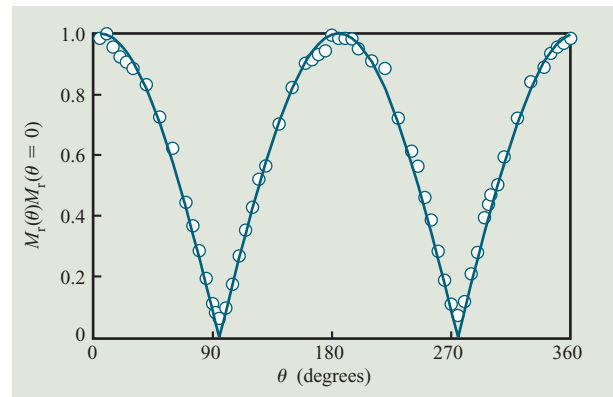
Figure 18

Dependence of remanent magnetization on the angle θ of the applied magnetic field with respect to the wire axis and the short diagonal in the ac plane. The solid curve corresponds to $SQ = SQ_0|\cos\theta|$. Adapted from [47], with permission.
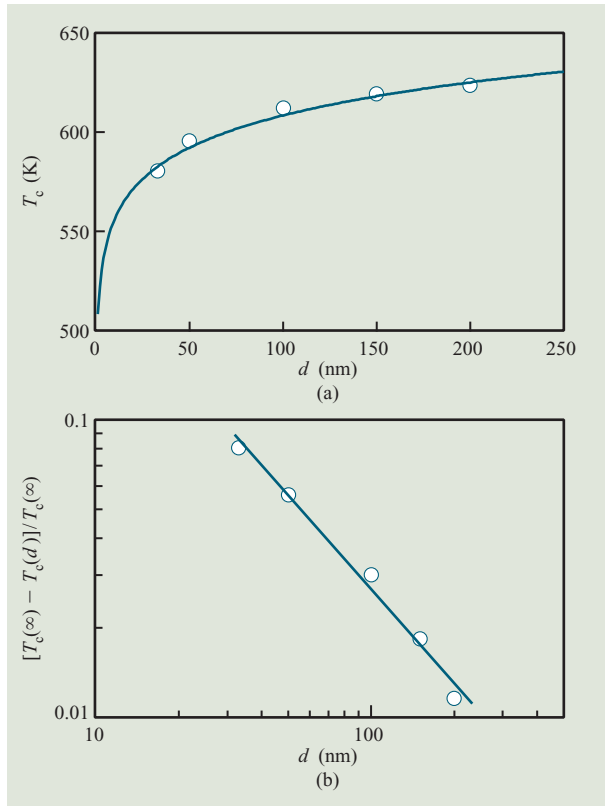

Figure 19

Dependence of coercivity on the angle θ of the applied magnetic field with respect to (o) the wire axis and the short diagonal in the ac plane and (Δ) the wire axis and the long diagonal in the bc plane for 120-nm-diameter nickel nanowires. The solid curve corresponds to $H_c = H_c(\theta = 0°)/\cos\theta$. Adapted from [47], with permission.

randomize the magnetization as a function of time. In superparamagnetic particles, the thermal energy overcomes the anisotropy energy; however, the thermal energy is still smaller than the exchange energy, and the magnetic moments are still aligned parallel to one another in the particles. The temperature at which the exchange energy between magnetic moments becomes smaller than the thermal energy and ferromagnetic order disappears is defined as the Curie temperature.

93

Figure 20

(a) Curie temperature of nickel nanowire arrays vs. wire diameter d, illustrating the decrease in T_c with decreasing diameter. (b) Log–log plot showing $[T_c(\infty) - T_c(d)]/T_c(\infty)$ normalized to the Curie temperature for bulk Ni $[T_c(\infty) = 631$ K] vs. wire diameter. The solid curve corresponds to $\lambda = 0.94$ and $\xi_0 = 22$ Å. Adapted from [75], with permission.

At 0 K, all magnetic moments are aligned along the same direction. When the temperature increases, spin-orientation fluctuations begin to occur. The distance over which fluctuations in the system are correlated is known as the correlation length ξ. In bulk magnetic systems, it increases with temperature and diverges at the bulk transition temperature $T_c(\infty)$, at which the magnetic disorder at one point randomizes the system and a ferromagnetic-to-paramagnetic phase transition occurs. When the physical dimensions of a system are reduced, finite size effects occur, changing the materials properties. In systems with reduced dimensions, the growth of ξ with temperature is limited by the smallest dimension d, and the system displays a reduced transition temperature $T_c(d)$ because of the finite-size effects.

Figure 20(a) shows the resulting decrease in the Curie temperature for nickel nanowires in mica templates [75]. The Curie temperature is reduced by about 50 K for a

nanowire diameter of 30 nm. Owing to the relatively large diameters, the nanowires are expected to behave as a constrained three-dimensional system.

The correlation length $\xi(T)$ of a magnetic system increases with temperature, and at temperatures close to the bulk transition temperature $T_c(\infty)$, it exhibits asymptotic behavior described by

$$\xi(T) = \xi_0 |1 - \frac{T}{T_c(\infty)}|^{-\nu}, \tag{47}$$

where ξ_0 is the correlation length extrapolated to $T = 0$, and ν is the critical exponent for correlation [76]. ξ_0 is typically of the order of the near-neighbor spacing, although for some ferromagnetic materials, such as nickel, it can be somewhat larger. For nanowires having a small diameter, the growth of $\xi(T)$ with increasing temperature is constrained by the wire diameter d, resulting in a reduced Curie temperature defined by

$$T_c(d) = T_c(\infty)\left[1 - \left(\frac{\xi_0}{d}\right)^\lambda\right] \tag{48}$$

or

$$\frac{T_c(\infty) - T_c(d)}{T_c(\infty)} = \left(\frac{\xi_0}{d}\right)^\lambda, \tag{49}$$

where $T_c(d)$ is the Curie temperature for nanowires with diameter d, and $\lambda = 1/\nu$ is the shift exponent.

Figure 20(b) shows a log–log plot of the reduced temperature $[T_c(\infty) - T_c(d)]/T_c(\infty)$ vs. wire diameter d, illustrating that the measured values for $T_c(d)$ follow the finite-size scaling relation. From this figure we obtain $\lambda = 0.94$ and an extrapolated value of $\xi_0 = 22$ Å. The observed exponent of $\lambda = 0.94$ is lower than the theoretical values predicted by the three-dimensional Heisenberg model ($\lambda = 1.4$) and the three-dimensional Ising model ($\lambda = 1.58$) [76, 77]; for both models, however, it is assumed that near-neighbor interactions occur, whereas nickel is a ferromagnet that exhibits longer-range interactions [78]. The extrapolated correlation length $\xi_0 = 22$ Å is close to the value of 20 Å reported for polycrystalline nickel thin films [79], although it is somewhat larger than the values of 4–10 Å obtained for epitaxial single-crystal nickel films [80, 81].

Multiple-segment nanowires

In previous sections we have discussed the influence of nanowire diameter on the magnetic properties of single-component nanowires. The magnetic properties of nanowires can be further modified in multiple-layer or multiple-segment nanowires consisting of ferromagnetic (FM) and nonmagnetic segments (NM) [82–92]. The magnetic properties of FM/NM multiple-layer (or

multilayer) nanowires can be precisely tuned by varying the size, aspect ratio, and spacing of the FM segments.

Electrodeposition of multilayer films from a solution containing the ions of two components is achieved by modulation of the potential or current and usually results in the deposition of a compositionally modulated multilayer with a bilayer repeat unit of the form A_xB_{1-x}/A_yB_{1-y}. Systems that have been studied include $Cu_xBi_{1-x}/Cu_yBi_{1-y}$ [93], $Cu_xZn_{1-x}/Cu_yZn_{1-y}$ [94], $Ni_xMo_{1-x}/Ni_yMo_{1-y}$ [95], $Ag_xPd_{1-x}/Ag_yPd_{1-y}$ [95], and $Au_xAg_{1-x}/Au_yAg_{1-y}$ [96]. In these systems, the compositional modulation was relatively small, typically less than 30 at.%.

A major breakthrough in multilayer deposition was associated with the recognition that multilayers of the form A_xB_{1-x}/A with $x \approx 0.01$ can be deposited for systems for which the difference in equilibrium potentials between A and B is sufficiently large (typically >0.4 V) and the concentration of the more noble component is very low (i.e., $[A^{n+}] \ll [B^{m+}]$). This approach has been successfully exploited in the deposition of films with alternating FM and NM layers that exhibit giant magnetoresistance (GMR). Examples of electrodeposited FM/NM multilayers include Ni/Cu [97–101], Co/Cu [102–106], CoNi/Cu [107–109], and NiFe/Cu [110–112].

Figure 21 shows a current vs. voltage curve for the electrodeposition of copper and nickel into the pores of a 6-μm-thick nanoporous polycarbonate membrane [91]. Electrodeposition was from a solution containing 0.5 mol/L $NiSO_4$, 0.005 mol/L $CuSO_4$, and 0.6 mol/L H_3BO_3. The equilibrium potentials for copper and nickel in this solution are $U_{eq}(Cu^{2+}/Cu) = 0.15$ V (vs. Ag/AgCl) and $U_{eq}(Ni^{2+}/Ni) = -0.468$ V (vs. Ag/AgCl). On scanning the potential negative from the open-circuit potential, the current onset at about $+0.05$ V is followed by a peak associated with the nucleation and diffusion-limited growth of copper. Because of the low Cu(II) concentration in solution, the deposition is diffusion-limited over a wide potential range. At more negative potentials, the onset of nickel deposition is seen at about -0.7 V. On the reverse scan the diffusion-limited deposition of copper is seen up to about 0 V, followed by a peak associated with the stripping of copper [99]. Note that nickel dissolution is negligible in this solution [87].

Figure 22(a) shows a transmission electron microscopy (TEM) bright-field image of part of a 120-nm-diameter $[Ni(20\ nm)/Cu(10\ nm)]_n$ multilayer nanowire. **Figure 22(b)** is an electron energy loss spectroscopy (EELS) image of part of a 30-nm-diameter $[Ni(4\ nm)/Cu(1\ nm)]_n$ multilayer nanowire. The layered structure and the reproducibility of the layer thickness are clearly seen.

For the multilayer nanowire shown in Figure 22(a), the Ni segments have an aspect ratio of 0.17, and
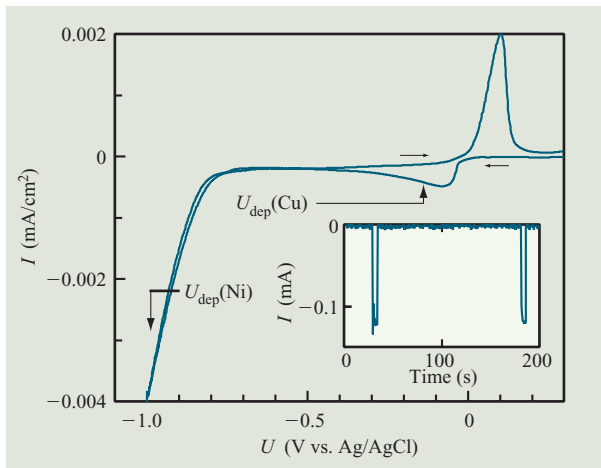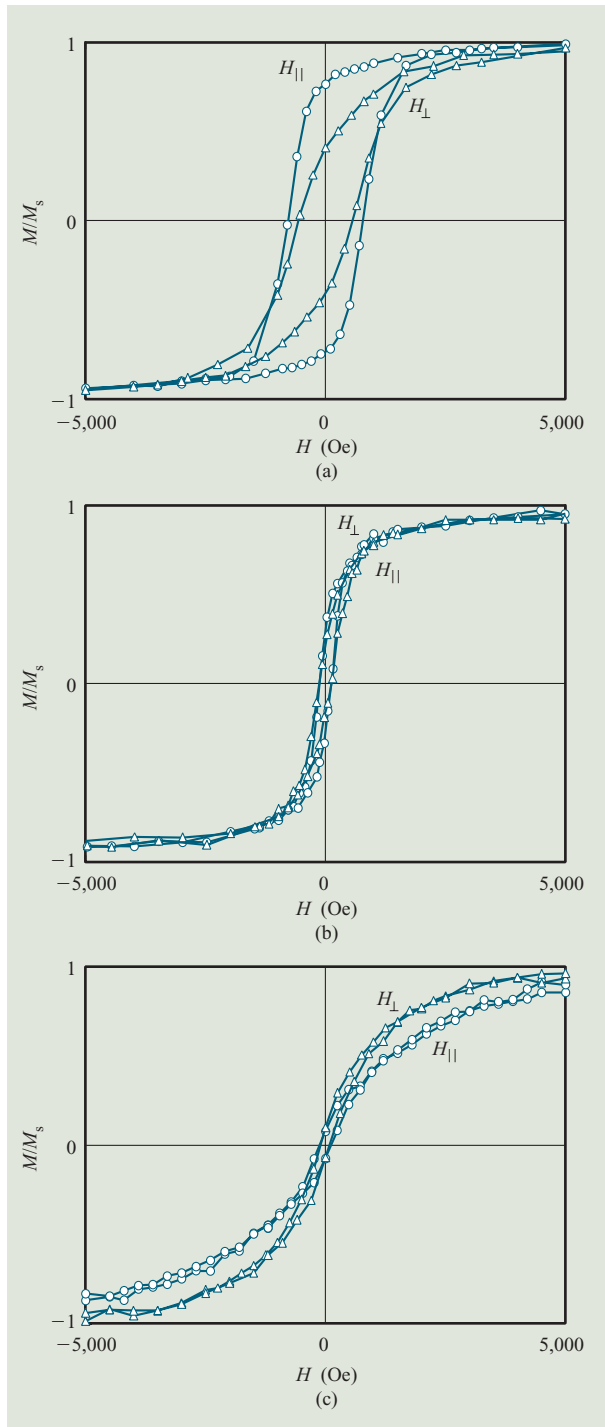

Figure 21

Current–voltage curve during electrodeposition onto a gold film at 10 mV/s through the pores of a 6-μm-thick nanoporous polycarbonate membrane [91]. Electrodeposition was from a solution containing 0.5 mol/L $NiSO_4$, 0.005 mol/L $CuSO_4$, and 0.6 mol/L H_3BO_3. The inset shows part of a current–time curve for the deposition of 50-nm-diameter $[Ni(125\ nm)/Cu(125\ nm)]_{10}$ multilayer nanowires. The two short (≈ 4 s) sections correspond to the deposition of Ni at -1.0 V, whereas the longer (≈ 140 s) section corresponds to the deposition of Cu at -0.16 V. From [92], with permission.
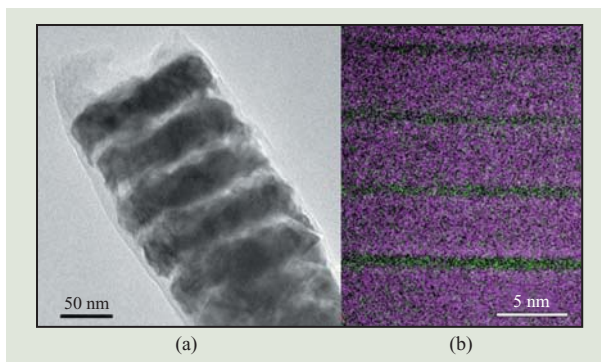
Figure 22

(a) TEM image of a 120-nm-diameter nanowire with 20-nm-thick Ni layers and 10-nm-thick Cu layers. (b) EELS image of a 30-nm-diameter nanowire with 1-nm-thick Ni layers and 4-nm-thick Cu layers. Adapted from [92], with permission.

from Equation (15) are expected to be single-domain. From the pore density, the average spacing between the nanowires in the templates is estimated to be 350–400 nm. These dimensions are sufficiently large to permit wire–wire interactions to be neglected.

95

Furthermore, the crystalline anisotropy of nickel is relatively small; hence, the magnetic response is dominated by the shape of the FM segments.

Figure 23 shows typical *M–H* loops for Ni/Cu multilayer nanowires. Figure 23(a) shows magnetization curves for 50-nm-diameter [Ni(125 nm)/Cu(125 nm)]$_{10}$ multilayer nanowires. For rod-shaped magnetic segments (aspect ratio > 1), the easy axis is parallel to the wire axis, as can be seen from the large remanence and coercivity. Perpendicular to the wire axis, the magnetization curves are characterized by very small remanences and coercivities. The measured saturation field along the hard axis is about 5,000 Oe, significantly larger than the value expected if only shape anisotropy is considered. $H_s = 1.73\pi M_s$ for an ellipsoid with an aspect ratio of 2.5, and $H_s = 2\pi M_s$ for an infinitely long cylinder. The larger saturation field indicates that intersegment interactions between the Ni segments along the length of the nanowires influence the magnetic response.

Figure 23(b) shows *M–H* curves for 100-nm-diameter [Ni(100 nm)/Cu(100 nm)]$_{30}$ multilayer nanowires. Here, the aspect ratio of the Ni segments is 1.0. The magnetization curves are essentially identical, with the applied field perpendicular or parallel to the wire axis. In both cases, the coercivity and remanence are very small and the saturation field is relatively large. Similar features have been reported for Ni cylinders with an aspect ratio close to 1.0; however, the coercivity and remanence are smaller for multilayer nanowires [114]. The saturation fields in both directions are close to the value of $4\pi M_s/3$ (2,030 Oe) for a sphere, indicating that in this case interlayer interactions are not significant.

Figure 23(c) shows *M–H* curves for 50-nm-diameter [Ni(5 nm)/Cu(5 nm)]$_{250}$ multilayer nanowires. In this case, with disk-shaped FM segments (aspect ratio = 0.1), the easy axis is perpendicular to the wire axis (parallel to the disk axis). The coercivity and remanence are small in both perpendicular and parallel orientations. Similar features have been reported for arrays of nickel disks [113, 114], although the saturation field for the multilayer nanowires is significantly larger. The saturation field along the hard axis (parallel to the wire axis) is about 5,300 Oe, close to the value of $3.44\pi M_s$ (5,241 Oe) for an oblate spheroid with an aspect ratio of 0.1; however, the saturation field along the easy axis is also large. These results show that dipolar interactions are also important for disk-shaped Ni segments.

The magnetic response of the arrays of multilayer nanowires can be represented on a micromagnetic phase diagram, similar to that used for two-dimensional arrays of single-component entities [114]. **Figure 24** shows a map of the three characteristic responses seen for the multilayer nanowires with rod-shaped FM segments (aspect ratio > 0.5, $d/\lambda_{ex} < 4$), disk-shaped FM segments

(aspect ratio < 0.5), and intermediate FM segments (aspect ratio > 0.5, $d/\lambda_{ex} > 4$). On the basis of micromagnetics simulations of isolated entities, these states have been referred to respectively as the out-of-plane flower state, the in-plane flower state, and the vortex state [114]. As can be seen from Figure 24, the magnetic response of the multilayer nanowires agrees reasonably well with the phase boundaries defined for the arrays of single-component elements, although the boundary between the rod-shaped segments and the disk-shaped segments is shifted to a lower aspect ratio for the multilayer nanowires.

The difference between the magnetic response of the multilayer FM/NM nanowires and two-dimensional arrays of FM entities is due to the dipolar magnetostatic interactions between the FM layers in the multilayer structures. For the multilayer nanowires with rod-shaped FM segments, magnetostatic interactions between the segments favor head-to-tail alignment of the magnetic moments along the wire axis. Thus, the remanence and coercivity along the easy axis (parallel to the wire axis) are larger than would be expected for a single FM rod of the same dimensions. In contrast, for multilayer nanowires with disk-shaped segments, magnetostatic interactions favor antiparallel alignment perpendicular to the wire axis. Thus, the remanence and coercivity along the easy axis (perpendicular to the wire axis) are smaller than would be obtained for a single disk. The shift in the boundary between the rod-shaped segments and the disk-shaped segments to a lower aspect ratio suggests that the head-to-tail alignment parallel to the wire axis is favored over the antiparallel alignment down to an aspect ratio of ~0.5.

In order to study the magnetostatic interlayer interaction in more detail, we fabricated a series of 50-nm-diameter [Ni(5 nm)/Cu(t nm)]$_n$ nanowires with Cu layer thickness ranging from 5 to 100 nm. In all samples the Ni segments were 5 nm thick, corresponding to an aspect ratio of 0.1. **Figure 25** shows the remanence measured with the field along the easy axis (perpendicular to the wire axis) vs. Cu layer thickness. The remanence increases from 0.09 to 0.26 as the Cu layer thickness increases from 5 to 100 nm, showing that the magnetostatic interaction between nickel segments decreases with increasing NM layer thickness.

Giant magnetoresistance

Figure 26(a) shows the M–H loop for 30-nm-diameter [Co(5 nm)/Cu(0.8 nm)]$_{1000}$ multilayer nanowires at 293 K with the field perpendicular to the wire axis [84]. The aspect ratio of the Co segments is 0.125; hence, the direction perpendicular to the wire axis is the magnetic easy axis. The [Co(5 nm)/Cu(x nm)]$_{200}$ multilayer nanowires were deposited from 50 g/L CoSO$_4$·6H$_2$O, 0.5 g/L CuSO$_4$·5H$_2$O, and 40 g/L boric acid [84].
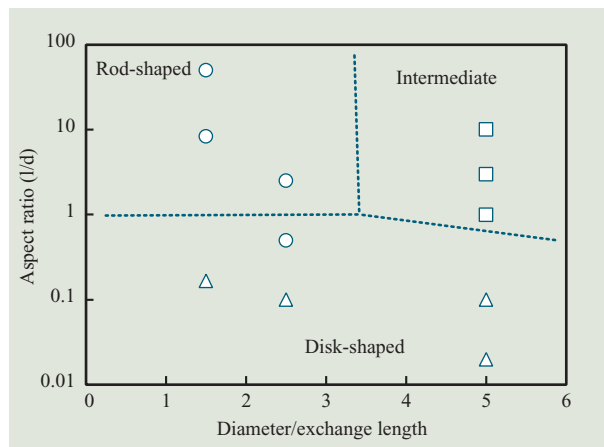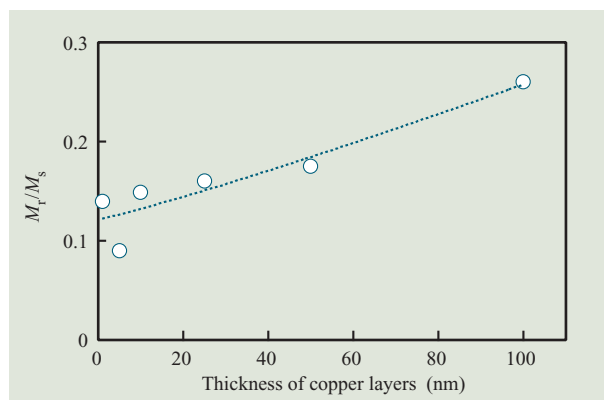
Cu and Co were deposited at −0.16 V (Ag/AgCl) and −1.00 V (Ag/AgCl), respectively. In order to minimize Co dissolution during the copper deposition cycle, a two-second segment at the open circuit potential was introduced into the deposition cycle after a Co deposition segment. At −0.16 V, only Cu is deposited, whereas at −1.00 V, the two metals are co-deposited. The concentration of copper in the cobalt layers was 7 at.%. Diffraction peaks up to the seventh order were observed in low-angle X-ray diffraction patterns, indicating good multilayer quality.

97
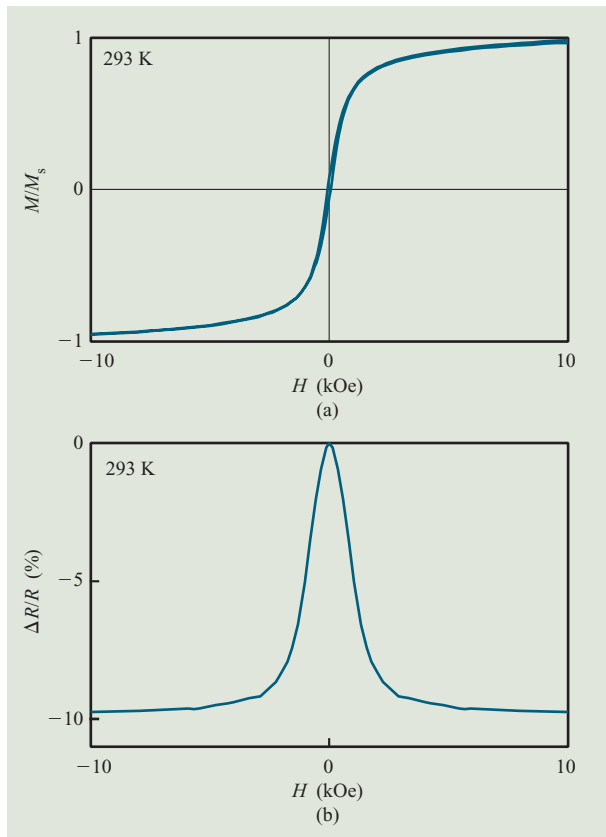
Figure 26

(a) *M–H* loop and (b) $\Delta R/R$–*H* curve for 30-nm-diameter [Co(5 nm)/Cu(0.8 nm)]$_{1,000}$ nanowires with the magnetic field perpendicular to the wire axis. Adapted from [84], with permission.
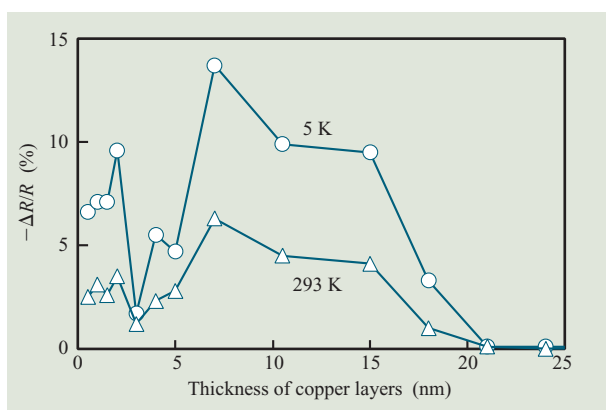
Figure 27

GMR effect for 400-nm-diameter [Co(5 nm)/Cu(*x* nm)]$_n$ multilayer nanowires at 5 K and 293 K vs. Cu layer thickness. Adapted from [84], with permission.

Figure 28

Optical microscope images of Ni/Cu multilayer nanowires suspended in a 1:1 octadecane and hexadecane mixture under an externally applied magnetic field. In both cases the nanowires are 100 nm in diameter and about 6 μm long, with an average composition of 50 at.% nickel, (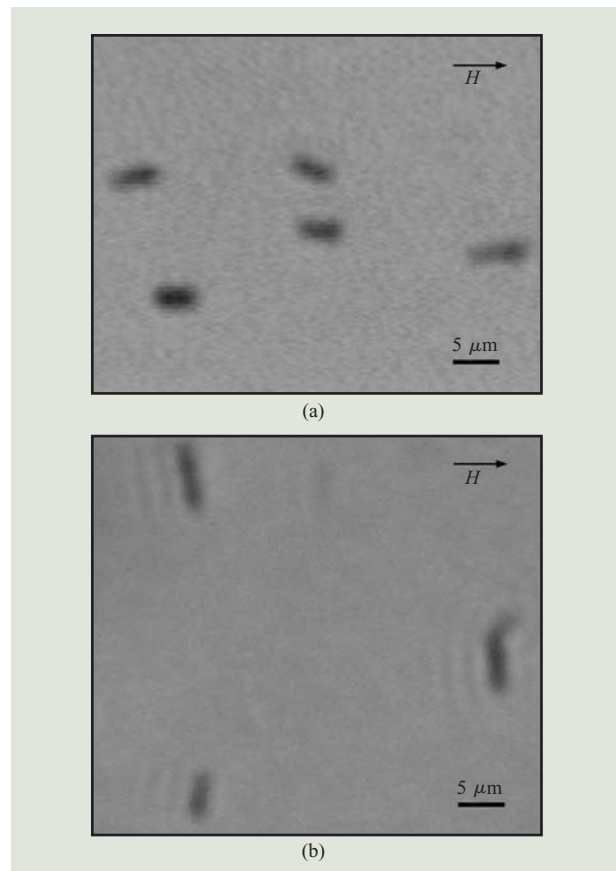a) [Ni(1,000 nm)/Cu(1,000 nm)]$_3$ with a diameter of 100 nm and (b) [Ni(10 nm)/Cu(10 nm)]$_{300}$ with a diameter of 100 nm. From [92], with permission.

Figure 26(b) shows the corresponding GMR effect plotted as the change is resistance-normalized with respect to the saturation resistance at 50 kOe. At room temperature, 11% GMR is observed with a zero field resistance of 38 Ω, with no discernible hysteretic characteristics.

Figure 27 shows a plot of the GMR effect at 5 K and 293 K for 400-nm-diameter [Co(5 nm)/Cu(*x* nm)]$_n$ multilayer nanowires vs. Cu layer thickness. As the Cu layer thickness increases, the GMR effect decreases; it approaches zero when the thickness approaches 21 nm. In this current-perpendicular-to-the-plane (CPP) geometry, the GMR effect is no longer observed when the copper layer thickness becomes comparable to the spin diffusion length (the length over which the conduction electron spin

is relaxed). When the Cu layer thickness exceeds the spin diffusion length, the spin of the conduction electrons is randomized as they pass through adjacent Co layers. Thus, from this figure, the spin diffusion length in copper is estimated to be about 21 nm. As can also be seen, for smaller Cu thicknesses (<10 nm), there appear to be clear oscillations of the GMR effect, a phenomenon well established in sputtered [115] and MBE-grown [116] Co/Cu multilayers.

Nanowire suspensions

Magnetic interactions between particles in suspension can influence the stability of the suspension and can be helpful in the assembly of larger-scale structures. For example, rod-shaped magnetic nanowires with high remanence can act as small bar magnets in suspension and can form one-dimensional chains because of the attractive wire–wire interactions [117, 118]. Nanowire suspensions can be formed by dissolving the template in a suitable solvent. For example, polycarbonate can be dissolved in dichloromethane. To ensure that the surface of each nanowire is clean, residual polycarbonate can be removed by sequential centrifugation and the addition of clean solvent, or by solvent exchange. The nanowires can then be suspended in water or an organic solvent.

The response of multilayer FM/NM nanowires in suspension to a small magnetic field can also be tailored by controlling the aspect ratio and thickness of the FM and NM layers [92]. **Figure 28** shows suspensions of Ni/Cu multilayer nanowires in a small ($\approx$10 Oe or 0.8 kA/m) external magnetic field. Figure 28(a) shows [Ni(1,000 nm)/Cu(1,000 nm)]$_3$ nanowires having a diameter of 100 nm and rod-shaped FM segments (aspect ratio = 10). The nanowires aligned parallel to the applied magnetic field, since their easy axis was parallel to their physical axis. Figure 28(b) shows [Ni(10 nm)/Cu(10 nm)]$_{300}$ nanowires of the same diameter and having disk-shaped FM segments (aspect ratio = 0.1). The nanowires had the same overall length and the same amount of nickel as those of part (a), but aligned perpendicular to the applied field, since their easy axis was perpendicular to their physical axis. These results illustrate that shape anisotropy can be exploited in tuning the response of magnetic nanoparticles in suspension.

Summary

A key requirement for using magnetic particles in specific applications is the ability to tailor their magnetic properties appropriately. In this paper we have reviewed the magnetic properties of single-component and multiple-segment magnetic nanowires and have provided examples of the influence of particle diameter, aspect ratio, and composition on many of their magnetic properties such as the orientation of the magnetic easy axis, the Curie temperature, coercivity, saturation field, saturation magnetization, and remanent magnetization.

References

1. R. E. Rosensweig, *Ferrohydrodynamics*, Dover, Mineola, New York, 1998.
2. E. Blums, A. Cebers, and M. M. Maiorov, *Magnetic Fluids*, de Gruyter, Berlin, 1997.
3. *Scientific and Clinical Applications of Magnetic Carriers*, U. Hafeli, W. Schutt, J. Teller, and M. Zborowshi, Eds., Plenum, New York, 1997.
4. *Magnetism in Medicine*, W. Andra and H. Nowak, Eds., Wiley, Berlin, 1998.
5. A. R. Bausch, W. Môller, and E. Sackmann, "Measurement of Local Viscoelasticity and Forces in Living Cells by Magnetic Tweezers," *Biophys. J.* **76**, 573–579 (1999).
6. C. Haber and D. Wirtz, "Magnetic Tweezers for DNA Micromanipulation," *Rev. Sci. Instrum.* **71**, 4561–4570 (2000).
7. T. R. Strick, J.-F. Allemand, D. Bensimon, and V. Croquette, "Behavior of Supercoiled DNA," *Biophys. J.* **74**, 2016–2028 (1998).
8. A. K. Salem, P. C. Searson, and K. W. Leong, "Multifunctional Nanorods for Gene Delivery," *Nature Mater.* **2**, 668–671 (2003).
9. C. Plank, U. Schillinger, F. Scherer, C. Bergemann, J. S. Remy, F. Krotz, M. Anton, J. Lausier, and J. Rosenecker, "The Magnetofection Method: Using Magnetic Force to Enhance Gene Delivery," *Biolog. Chem.* **384**, 737–747 (2003).
10. F. Scherer, M. Anton, U. Schillinger, J. Henkel, C. Bergemann, A. Kruger, B. Gansbacher, and C. Plank, "Magnetofection: Enhancing and Targeting Gene Delivery by Magnetic Force In Vitro and In Vivo," *Gene Therapy* **9**, 102–109 (2002).
11. X. W. Wu, H. Zhou, R. J. M. van de Veerdonk, T. J. Klemmer, C. Liu, N. Shukla, D. Weller, M. Tanase, and D. E. Laughlin, "Studies of Switching Field and Thermal Energy Barrier Distributions in a FePt Nanoparticle System," *J. Appl. Phys.* **93**, 7181–7183 (2003).
12. S. Sun, C. B. Murray, D. Weller, L. Folks, and A. Moser, "Monodisperse FePt Nanoparticles and Ferromagnetic FePt Nanocrystal Superlattices," *Science* **287**, 1989–1992 (2000).
13. G. E. Possin, "A Method for Forming Very Small Diameter Wires," *Rev. Sci. Instrum.* **41**, 772–774 (1970).
14. G. E. Possin, "Superconductivity in Nearly One Dimensional Tin Wires," *Physica* **55**, 339–343 (1971).
15. C. R. Martin, "Nanomaterials: A Membrane-Based Synthetic Approach," *Science* **266**, 1961–1965 (1994).
16. Y. Xia, P. Yang, Y. Sun, Y. Wu, B. Mayers, B. Gates, Y. Yin, F. Kim, and H. Yan, "One Dimensional Nanostructures: Synthesis, Characterization, and Applications," *Adv. Mater.* **15**, 353 (2003).
17. W. D. Williams and N. Giordano, "Experimental Study of Localization and Electron–Electron Interaction Effects in Thin Au Wires," *Phys. Rev. B* **33**, 8146 (1986).
18. D. Routkevitch, T. Bigioni, M. Moskovits, and J. M. Xu, "Electrochemical Fabrication of CdS Nanowire Arrays in Porous Anodic Aluminum Oxide Templates," *J. Phys. Chem.* **100**, 14037–14047 (1996).

99

19. D. N. Davydov, P. A. Sattari, D. Al Mawlawi, A. Osika, T. L. Haslett, and M. Moskovits, "Field Emitters Based on Porous Aluminum Oxide Templates," *J. Appl. Phys.* **86**, 3983–3987 (1999).

20. K. Liu, C. L. Chien, P. C. Searson, and K. Yu-Zhang, "Structural and Magneto Transport Properties of Electrodeposited Bismuth Nanowires," *Appl. Phys. Lett.* **73**, 1436 (1998).

21. K. Liu, C. L. Chien, and P. C. Searson, "Finite Size Effects in Electrodeposited Bismuth Nanowires," *Phys. Rev. B* **58**, 14681 (1998).

22. K. B. Shelimov, D. N. Davydov, and M. Moskovits, "Template-Grown High-Density Nanocapacitor Arrays," *Appl. Phys. Lett.* **77**, 1722–1724 (2000).

23. G. Patermarakis and K. Moussoutzanis, "Mathematical Models for the Anodization Conditions and Structural Features of Porous Anodic Al_2O_3 Films on Aluminum," *J. Electrochem. Soc.* **142**, 737 (1995).

24. G. Patermarakis, "Development of a Theory for the Determination of the Composition of the Anodizing Solution Inside the Pores During Growth of Porous Anodic Al_2O_3 Films on Aluminum by a Transport Phenomenon Analysis," *J. Electroanal. Chem.* **447**, 25 (1998).

25. L. Ba and W. S. Li, "Influence of Anodizing Conditions on the Ordered Pore Formation in Anodic Alumina," *J. Phys. D: Appl. Phys.* **33**, 2527–2531 (2000).

26. H. Masuda, H. Yamada, M. Satoh, H. Asoh, M. Nakao, and T. Tamamura, "Highly Ordered Nanochannel Array Architecture in Anodic Alumina," *Appl. Phys. Lett.* **71**, 2770 (1997).

27. S. Shingubara, O. Okino, Y. Sayama, H. Sakaue, and T. Takahagi, "Two Dimensional Nanowire Array Formation on Silicon Using Self-Organized Nanoholes of Anodically Oxidized Aluminum," *Solid State Electron.* **43**, 1143–1146 (1999).

28. O. Jessensky, F. Muller, and U. Goesele, "Self-Organized Formation of Hexagonal Pore Arrays in Anodic Alumina," *Appl. Phys. Lett.* **72**, 1173 (1998).

29. A. P. Li, F. Muller, K. Nielsch, and U. Goesele, "Polycrystalline Nanopore Arrays with Hexagonal Ordering on Aluminum," *J. Vac. Sci. Technol. A* **17**, 1428 (1999).

30. A. P. Li, F. Muller, A. Birner, K. Nielsch, and U. Goesele, "Hexagonal Pore Arrays with a 50–420 nm Interpore Distance Formed by Self-Organization in Anodic Alumina," *J. Appl. Phys.* **84**, 6023 (1998).

31. K. Nielsch, F. Muller, A. P. Li, and U. Goesele, "Uniform Nickel Deposition into Ordered Alumina Pores by Pulsed Electrodeposition," *Adv. Mater.* **12**, 582 (2000).

32. H. Masuda, K. Yasui, Y. Sakamoto, M. Nakao, T. Tamamura, and K. Nishio, "Ideally Ordered Anodic Porous Alumina Mask Prepared by Imprinting of Vacuum Evaporated Al on Si," *Jpn. J. Appl. Phys.* **40**, L1267–L1268 (2001).

33. J. S. Choi, R. B. Wehrspohn, and U. Gosele, "Moire Pattern Formation on Porous Alumina Arrays Using Nanoimprint Lithography," *Adv. Mater.* **15**, 1531 (2003).

34. R. L. Fleischer, P. B. Price, and R. M. Walker, *Nuclear Tracks in Solids*, University of California Press, Berkeley, 1975.

35. B. E. Fischer and R. Spohr, "Production and Use of Nuclear Tracks: Imprinting Structure on Solids," *Rev. Mod. Phys.* **55**, 907 (1983).

36. J. A. Quinn, J. L. Anderson, W. S. Ho, and W. J. Petzny, "Model Pores of Molecular Dimensions," *Biophys. J.* **12**, 990 (1970).

37. P. B. Price and R. M. Walker, "Observations of Charged-Particle Tracks in Solids," *J. Appl. Phys.* **33**, 3400 (1962).

38. P. B. Price and R. M. Walker, "Chemical Etching of Charged-Particle Tracks in Solids," *J. Appl. Phys.* **33**, 3407 (1962).

39. C. P. Bean, M. V. Doyle, and G. Entine, "Etching Submicron Pores in Irradiated Mica," *J. Appl. Phys.* **41**, 1454–1459 (1970).

40. G. Guillot and F. Rondelelz, "Characteristics of Submicron Pores Obtained by Chemical Etching of Nuclear Tracks in Polycarbonate Films," *J. Appl. Phys.* **52**, 7155–7164 (1981).

41. S. K. Chakarvarti and J. Vetter, "Morphology of Etched Pores and Microstructures Fabricated from Nuclear Track Filters," *Nucl. Instrum. & Meth. B* **62**, 109 (1991).

42. L. Sun, C. L. Chien, and P. C. Searson, "Fabrication of Nanoporous Single Crystal Mica Templates for Electrochemical Deposition of Nanowire Arrays," *J. Mater. Sci.* **35**, 1079 (2000).

43. T. Thurn-Albrecht, J. Schotter, G. A. Kastle, N. Emley, T. Shibauchi, L. Krusin-Elbaum, K. Guarini, C. T. Black, M. T. Tuominen, and T. P. Russell, "Ultrahigh Density Nanowire Arrays Grown in Self-Assembled Diblock Copolymer Templates," *Science* **290**, 2126 (2000).

44. U. Y. Jeong, D. Y. Ryu, J. K. Kim, D. H. Kim, X. D. Wu, and T. P. Russell, "Precise Control of Nanopore Size in Thin Film Using Mixtures of Asymmetric Block Copolymer and Homopolymer," *Macromolecules* **36**, 10126–10129 (2003).

45. M. Bal, A. Ursache, M. T. Tuominen, J. T. Goldbach, and T. P. Russell, "Nanofabrication of Integrated Magnetoelectronic Devices Using Patterned Self-Assembled Copolymer Templates," *Appl. Phys. Lett.* **81**, 3479–3481 (2002).

46. T. M. Whitney, J. S. Jiang, P. C. Searson, and C. L. Chien, "Fabrication and Magnetic Properties of Arrays of Metallic Nanowires," *Science* **261**, 1316 (1993).

47. L. Sun, P. C. Searson, and C. L. Chien, "Magnetic Anisotropy in Prismatic Nickel Nanowires," *Appl. Phys. Lett.* **79**, 4429 (2001).

48. W. F. Brown, *Micromagnetics*, Wiley, New York, 1963.

49. R. D. Cullity, *Introduction to Magnetic Materials*, Addison-Wesley, Reading, MA, 1972.

50. E. H. Frei, S. Shtrikman, and D. Treves, "Critical Size and Nucleation Field of Ideal Ferromagnetic Particles," *Phys. Rev.* **106**, 446 (1957).

51. A. Aharoni, *Introduction to the Theory of Ferromagnetism*, Oxford University Press, New York, 1996.

52. E. C. Stoner and E. P. Wohlfarth, "A Mechanism of Magnetic Hysteresis in Heterogeneous Alloys," *Phil. Trans. Roy. Soc. Lond. A* **240**, 599–642 (1948). Republished in *IEEE Trans. Magn.* **27**, 3475–3518 (1991).

53. A. Aharoni, "Angular Dependence of Nucleation by Curling in a Prolate Spheroid," *J. Appl. Phys.* **82**, 1281 (1997).

54. M. E. Schabes, "Micromagnetic Theory of Nonuniform Magnetization Processes in Magnetic Recording Particles," *J. Magn. Magn. Mater.* **95**, 249 (1991).

55. J. E. Wegrowe, D. Kelly, A. Franck, S. E. Gilbert, and J. Ph. Ansermet, "Magnetoresistance of Ferromagnetic Nanowires," *Phys. Rev. Lett.* **82**, 3681 (1999).

56. R. C. O'Handley, *Modern Magnetic Materials*, Wiley, New York, 2000, p. 74.

57. M. P. Sharrock, "Time Dependence of Switching Fields in Magnetic Recording Media," *J. Appl. Phys.* **76**, 6413–6418 (1994).

58. H. Q. Yin and W. D. Doyle, "Thermal Relaxation in Soft Magnetic Patterned Elements," *J. Appl. Phys.* **91**, 7709–7711 (2002).

59. L. Cheng-Zhang and L. C. Lodder, "The Influence of Packing Density on the Magnetic Behavior of Alumite Media," *J. Magn. Magn. Mater.* **88**, 236 (1990).

60. D. J. Selmeyer, M. Zhang, and R. Skomski, "Magnetism of Fe, Co, and Ni Nanowires in Self-Assembled Arrays," *J. Phys.: Condens. Matter* **13**, R433–R460 (2001).

61. N. Tsuya, Y. Saito, N. Nakamura, S. Hayano, A. Furugohri, K. Ohta, Y. Wakui, and T. Tokushima, "A Perpendicular Magnetic Recording Medium by Alumite," *J. Magn. Magn. Mater.* **54–57**, 1681 (1986).

62. G. T. A. Huysmans, J. C. Lodder, and J. Wakui, "Magnetization Curling in Perpendicular Iron Particle Arrays," *J. Appl. Phys.* **64**, 2016 (1988).

100

63. D. Al Malawi, N. Coombs, and M. Moskovits, "Magnetic Properties of Fe Deposited into Anodic Aluminum Oxide Pores as a Function of Particle Size," *J. Appl. Phys.* **70**, 4421 (1991).

64. J. Meier, B. Doudin, and J. P. Ansermet, "Magnetic Properties of Nanosized Wires," *J. Appl. Phys.* **79**, 6010 (1996).

65. C. Beeli, B. Doudin, J. P. Ansermet, and P. Stadelmann, "Study of Co, Ni and Co/Cu Nanowires: Magnetic Flux Imaging by Off-Axis Electron Holography," *J. Magn. Magn. Mater.* **164**, 77–90 (1996).

66. W. Wernsdorfer, B. Doudin, D. Mailly, K. Hasselbach, A. Benoit, J. Meier, J.-Ph. Ansermet, and B. Barbara, "Magnetoresistance of Ferromagnetic Nanowires" *Phys. Rev. Lett.* **77**, 1873 (1996).

67. R. O'Barr and S. Schultz, "Switching Field Studies of Individual Single Domain Ni Columns," *J. Appl. Phys.* **81**, 5458 (1997).

68. R. Ferre, K. Ounadjela, J. M. George, L. Piraux, and S. Dubois, "Magnetization Processes in Nickel and Cobalt Electrodeposited Nanowires," *Phys. Rev. B* **56**, 14066 (1997).

69. L. Piraux, S. Dubois, E. Ferain, R. Legras, K. Ounadjela, J. M. George, J. L. Maurice, and A. Fert, "Anisotropic Transport and Magnetic Properties of Arrays of Submicron Wires," *J. Magn. Magn. Mater.* **165**, 352–355 (1997).

70. L. Sun, P. C. Searson, and C. L. Chien, "Electrochemical Deposition of Nickel Nanowire Arrays in Single Crystal Mica Films," *Appl. Phys. Lett.* **74**, 2803 (1999).

71. J. Wegrowe, D. Kelly, Y. Jaccard, P. Guittienne, and J. P. Ansermet, "Current-Induced Magnetization Reversal in Magnetic Nanowires," *Europhys. Lett.* **45**, 626 (1999).

72. S. Dubois, E. Chassaing, J. L. Duvail, L. Piraux, and M. G. Waals, "Preparation and Characterization of Electrodeposited Fe and Fe/Cu Nanowires," *J. Chim. Phys.* **96**, 1316–1331 (1999).

73. Y. Jaccard, P. Guittienne, D. Kelly, J. E. Wegrowe, and J. P. Ansermet, "Uniform Magnetization Rotation in Single Ferromagnetic Nanowires," *Phys. Rev. B* **62**, 1141–1147 (2000).

74. S. Pignard, G. Goglio, A. Radulescu, L. Piraux, S. Dubois, A. Declemy, and J. L. Duvail, "Study of the Magnetization Reversal in Individual Nickel Nanowires," *J. Appl. Phys.* **87**, 824 (2000).

75. L. Sun, C. L. Chien, and P. C. Searson, "Finite Size Effects in Nickel Nanowire Arrays," *Phys. Rev. B, Rapid Commun.* **61**, R6463 (2000).

76. See for example H. E. Stanley, *Introduction to Phase Transitions and Critical Phenomena*, Oxford University Press, New York, 1971, p. 46.

77. C. M. Schneider, P. Bressler, P. Schuster, J. Kirschner, J. J. de Miguel, and R. Miranda, "Curie-Temperature of Ultrathin Films of fcc Cobalt Epitaxially Grown on Atomically Flat Cu(100) Surfaces," *Phys. Rev. Lett.* **64**, 1059 (1990).

78. S. N. Kaul, "Low-Temperature Magnetization and Spin-Wave Excitations in Amorphous Ni-Rich Transition-Metal-Metalloid Alloys," *Phys. Rev. B* **27**, 5761–5774 (1983).

79. H. Lutz, J. D. Gunton, H. J. K. Schurmann, J. E. Crow, and T. Mihalisin, "The Influence of Finite Size on Critical Phenomena in Ni Films," *Solid State Commun.* **14**, 1075–1078 (1974).

80. R. Bergholz and V. Gradmann, "Structure and Magnetism of Oligatomic Ni(111)-Films on Re(0001)," *J. Magn. Magn. Mater.* **45**, 389–398 (1984).

81. F. Huang, G. J. Mankey, M. T. Kief, and R. F. Willis, "Finite-Size Scaling Behavior of Ferromagnetic Thin Films," *J. Appl. Phys.* **73**, 6760 (1993).

82. L. Piraux, J. M. George, J. F. Despres, C. Leroy, E. Ferain, R. Legras, K. Ounadjela, and A. Fert, "Giant Magnetoresistance in Magnetic Multilayered Nanowires," *Appl. Phys. Lett.* **65**, 2484 (1994).

83. A. Blondel, J. P. Meier, B. Boudin, and J.-Ph. Ansermet, "Giant Magnetoresistance of Nanowires of Multilayers," *Appl. Phys. Lett.* **65**, 3019 (1994).

84. K. Liu, K. Nagodawithana, P. C. Searson, and C. L. Chien, "Perpendicular Giant Magnetoresistance of Electrodeposited Co/Cu Layered Nanowires," *Phys. Rev. B, Rapid Commun.* **51**, 7381 (1995).

85. J. L. Maurice, D. Imhoff, P. Etienne, O. Durand, S. Dubois, L. Piraux, J. M. George, P. Galtier, and A. Fert, "Microstructure of Magnetic Metallic Superlattices Grown by Electrodeposition in Membrane Nanopores," *J. Magn. Magn. Mater.* **184**, 1–18 (1998).

86. S. Dubois, L. Piraux, J. M. George, K. Ounadjela, J. L. Duvail, and A. Fert, "Evidence for a Short Spin Diffusion Length in Permalloy from the Giant Magnetoresistance of Multilayered Nanowires," *Phys. Rev. B* **60**, 477 (1999).

87. L. Piraux, S. Dubois, C. Marchal, J. M. Beuken, L. Filipozzi, J. F. Depres, K. Ounadjela, and A. Fert, "Perpendicular Magnetoresistance in Co/Cu Multilayered Nanowires," *J. Magn. Magn. Mater.* **156**, 317–320 (1996).

88. S. Dubois, C. Marchal, J. M. Beuken, L. Piraux, J. L. Duvail, A. Fert, J. M. George, and J. L. Maurice, "Perpendicular Giant Magnetoresistance of NiFe/Cu Multilayered Nanowires," *Appl. Phys. Lett.* **70**, 396 (1997).

89. L. Piraux, S. Dubois, A. Fert, and L. Belliard, "The Temperature Dependence of the Perpendicular Giant Magnetoresistance in Co/Cu Multilayered Nanowires," *Euro. Phys. J.* **B4**, 413–420 (1998).

90. P. R. Evans, G. Yi, and W. Schwarzacher, "Current Perpendicular to Plane Giant Magnetoresistance of Multilayered Nanowires Electrodeposited in Anodic Aluminum Oxide Membranes," *Appl. Phys. Lett.* **76**, 481–483 (2000).

91. M. Chen, P. C. Searson, and C. L. Chien, "Micromagnetic Behavior of Electrodeposited Ni/Cu Multilayer Nanowires," *J. Appl. Phys.* **93**, 8253–8255 (2003).

92. M. Chen, L. Sun, J. E. Bonevich, D. H. Reich, C. L. Chien, and P. C. Searson, "Tuning the Response of Magnetic Suspensions," *Appl. Phys. Lett.* **82**, 3310–3312 (2003).

93. A. Brenner, *Electrodeposition of Alloys*, Vol. II, Academic Press, New York, 1963, p. 589.

94. R. Weil, C. C. Nee, and J. W. Chang, "Pulsed Electrodeposition of Layered Brass Structures," *Metall. Trans. A* **19**, 1569–1573 (1988).

95. C. C. Nee, W. Kim, and R. Weil, "Pulsed Electrodeposition of Ni–Mo Alloys," *J. Electrochem. Soc.* **135**, 1100–1103 (1988).

96. C. Ji, G. Oskam, Y. Ding, J. D. Erlebacher, A. J. Wagner, and P. C. Searson, "Deposition of $Au_xAg_{1-x}/Au_yAg_{1-y}$ Multilayers and Multisegment Nanowires," *J. Electrochem. Soc.* **150**, C523–C528 (2003).

97. D. S. Lashmore and M. P. Dariel, "Electrodeposited Cu–Ni Textured Superlattices," *J. Electrochem. Soc.* **135**, 1218–1221 (1988).

98. A. R. Despic, V. D. Jovic, and S. Spaic, "Electrochemical Formation of Laminar Deposits of Controlled Structure and Composition: 2. Dual Current Pulse Galvanostatic Technique," *J. Electrochem. Soc.* **136**, 1651–1657 (1989).

99. D. M. Tench and J. T. White, "Considerations in Electrodeposition of Compositionally Modulated Alloys," *J. Electrochem. Soc.* **137**, 3061–3066 (1990).

100. C. Bonhôte and D. Landolt, "Microstructure of Ni–Cu Multilayers Electrodeposited from a Citrate Electrolyte," *Electrochim. Acta* **42**, 2407–2417 (1997).

101. T. Miyake, M. Kume, K. Yamaguchi, D. Amalnerkar, and H. Minoura, "Electrodeposition of Cu/Ni–P Multilayers by a Single Bath Technique," *Thin Solid Films* **397**, 83–89 (2001).

102. M. Dariel, L. H. Bennet, D. S. Lashmore, P. Lubitz, M. Rubenstein, W. L. Lechter, and M. Z. Harford, "Properties of Electrodeposited Co–Cu Multilayer Structures," *J. Appl. Phys.* **61**, 4067 (1987).

101

103. R. D. McMichael, U. Atzmony, C. Beauchamp, L. H. Bennet, L. J. Swartzendruber, D. S. Lashmore, and L. T. Romankiw, "Fourfold Anisotropy of an Electrodeposited Co/Cu Compositionally Modulated Alloy," *J. Magn. Magn. Mater.* **113**, 149–154 (1992).

104. S. K. J. Lenczowski, C. Schonenberger, M. A. M. Gijs, and W. J. M. de Jonge, "Giant Magnetoresistance of Electrodeposited Co/Cu Multilayers," *J. Magn. Magn. Mater.* **148**, 455–465 (1995).

105. Y. Jyoko, S. Kashiwabara, and Y. Hayashi, "Characterization of Electrodeposited Co/Cu Ultrathin Films and Multilayers," *J. Magn. Magn. Mater.* **165**, 280–283 (1997).

106. S. Dubois, J. M. Beuken, L. Piraux, J. L. Duvail, A. Fert, J. M. George, and J. L. Maurice, "Perpendicular Giant Magnetoresistance of NiFe/Cu and Co/Cu Multilayered Nanowires," *J. Magn. Magn. Mater.* **165**, 30–33 (1997).

107. M. Alper, P. S. Aplin, K. Attenborough, D. J. Dingley, R. Hart, S. J. Lane, D. S. Lashmore, and W. Schwarzacher, "Growth and Characterization of Electrodeposited Cu/Cu–Ni–Co Alloy Superlattices," *J. Magn. Magn. Mater.* **126**, 8–11 (1993).

108. S. Z. Hua, D. S. Lashmore, L. Salamanca-Riba, W. Schwarzacher, L. J. Swartzendruber, R. D. McMichael, L. H. Bennet, and R. Hart, "Giant Magnetoresistance Peaks in CoNiCu/Cu Multilayers Grown by Electrodeposition," *J. Appl. Phys.* **76**, 6519–6521 (1994).

109. W. Schwarzacher, K. Attenborough, A. Michel, G. Nabiyouni, and J. P. Meier, "Electrodeposited Nanostructures," *J. Magn. Magn. Mater.* **165**, 23–29 (1997).

110. K. Attenborough, R. Hart, S. J. Lane, M. Alper, and W. Schwarzacher, "Magnetoresistance in Electrodeposited Ni–Fe–Cu/Cu multilayers," *J. Magn. Magn. Mater.* **148**, 335–336 (1995).

111. J. Yahalom and O. Zadok, "Formation of Composition-Modulated Alloys by Electrodeposition," *J. Mater. Sci.* **22**, 499–503 (1987).

112. J. Yahalom and O. Zadok, "Method for the Production of Alloys Possessing High Elastic Modulus and Improved Magnetic Properties by Electrodeposition," U.S. Patent 4,652,348, 1987.

113. C. A. Ross, R. Chantrell, M. Hwang, M. Farhoud, T. A. Savas, Y. Hao, H. I. Smith, F. M. Ross, M. Redjdal, and F. B. Humphrey, "Incoherent Magnetization Reversal in 30-nm Ni Particles," *Phys. Rev. B.* **62**, 14252–14258 (2000).

114. C. A. Ross, M. Hwang, M. Shima, J. Y. Cheng, M. Farhoud, T. A. Savas, H. I. Smith, W. Schwarzacher, F. M. Ross, M. Redjdal, and F. B. Humphrey, "Micromagnetic Behavior of Electrodeposited Cylinder Arrays," *Phys. Rev. B* **65**, 14417 (2002).

115. S.-F. Lee, W. P. Pratt, Jr., Q. Yang, P. Holody, R. Loloee, P. A. Schroeder, and J. Bass, "Two-Channel Analysis of CPP-MR Data for Ag/Co and AgSn/Co Multilayers," *J. Magn. Magn. Mater.* **118**, L1–L5 (1993).

116. M. T. Johnson, S. T. Purcell, N. W. E. McGee, R. Coehoorn, J. aan de Stegge, and W. Hoving, "Structural Dependence of the Oscillatory Exchange Interaction Across Cu Layers," *Phys. Rev. Lett.* **68**, 2688–2691 (1992).

117. M. Tanase, L. Bauer, A. Hultgren, D. M. Silevitch, L. Sun, D. H. Reich, P. C. Searson, and G. J. Meyer, "Magnetic Alignment of Fluorescent Nanowires," *Nano Lett.* **1**, 155–158 (2001).

118. C. L. Chien, L. Sun, M. Tanase, L. A. Bauer, A. Hultgren, D. M. Silevitch, G. J. Meyer, P. C. Searson, and D. H. Reich, "Electrodeposited Magnetic Nanowires: Arrays, Field-Induced Assembly, and Surface Functionalization," *J. Magn. Magn. Mater.* **249**, 146–155 (2002).

102

Li Sun *Department of Mechanical Engineering, University of Houston, Houston, Texas 77057 (lsun4@uh.edu).* Dr. Sun is the Bill D. Cook Assistant Professor in the Materials Science program at the University of Houston. He received a Ph.D. degree in materials science and engineering from Johns Hopkins University in 2002 and was a Postdoctoral Research Fellow in the Materials Research Science and Engineering Center at Hopkins until 2003.

Yaowu Hao *Department of Materials Science and Engineering, Johns Hopkins University, Baltimore, Maryland 21218 (yhao@jhu.edu).* Dr. Hao is a Postdoctoral Fellow in the Department of Materials Science and Engineering at Johns Hopkins University. He received a Ph.D. degree in materials science and engineering from MIT in 2003.

Chia-Ling Chien *Department of Physics and Astronomy, Johns Hopkins University, Baltimore, Maryland 21218 (clc@pha.jhu.edu).* Dr. Chien is the Jacob L. Hain Professor of Physics in the Department of Physics and Astronomy at Johns Hopkins University. He received a Ph.D. degree in 1973 from Carnegie-Mellon University.

Peter C. Searson *Department of Materials Science and Engineering, Johns Hopkins University, Baltimore, Maryland 21218 (searson@jhu.edu).* Dr. Searson is a Professor of Materials Science and Engineering in the Department of Materials Science and Engineering at Johns Hopkins University. He received a Ph.D. degree in 1982 from the University of Manchester Institute of Science and Technology and was a Research Associate at MIT until 1990.